Measuring Volcanic Plume and Ash Properties from Space

R.G. Grainger[*1], D.M. Peters[1], G.E. Thomas[1], A.J.A. Smith[1],
R. Siddans[2], E. Carboni[1], and A. Dudhia[1]

[1]Sub-Department of Atmospheric, Oceanic and Planetary
Physics, University of Oxford, Parks Road, Oxford, OX1 3PU,
England
[2]Science and Technology Facilities Council Rutherford
Appleton Laboratory, Harwell Science and Innovation Campus,
Didcot, OX11 0QX, England
[*]Corresponding author(email:r.grainger@physics.ox.ac.uk)

Number of Words:10,416
Abbreviated Title: Volcanic Plume and Ash Properties

Abstract: The remote sensing of volcanic ash plumes from space can provide a warning of an aviation hazard and knowledge on eruption processes and radiative effects. In this paper new algorithms are presented to provide volcanic plume properties from measurements by the Michelson Interferometer for Passive Atmospheric Sounding (MIPAS), the Advanced Along Track Scanning Radiometer (AATSR) and Spinning Enhanced Visible and Infrared Imager (SEVIRI). A challenge of remote sensing is to provide near real-time methods to identify, and so warn, of the presence of volcanic ash. To achieve this, a singular vector decomposition method has been developed for the MIPAS instrument on board the Environmental Satellite (ENVISAT). This method has been applied to observations of the ash clouds from the eruptions of Nabro and the Puyehue-Cordón Caulle in 2011 and lead to a more sensitive volcanic signal flag which was capable of tracking changes in the volcanic signal spectra as the plume evolved. A second challenge for remote sensing is to identify the ash plume height. This is a critical parameter for the initialisation of algorithms that numerically model the evolution and transport of a volcanic plume. As MIPAS is a limb sounder the identification of ash also provides an estimate of height provided the plume is above about 6 km. This is complemented by a new algorithm, Stereo Ash Plume Height Retrieval Algorithm (SAPHRA), that identifies plume height using the parallax between images provided by Along Track Scanning Radiometer type instruments. The algorithm was tested on an image taken at 14:01 GMT on 6 June 2011 of the Puyehue-Cordón Caulle eruption plume and gives a height of 11.9 ± 1.4 km which agreed with the value derived from the location of the plume shadow (12.7 ± 1.8 km). This plume height was similar to the height observed by MIPAS (12 ± 1.5 km) at 02:56 GMT on 6 June. The quantitative use of satellite imagery and the full exploitation of high resolution spectral measurements of ash depends upon knowing the optical properties of the observed ash. Laboratory measurements of ash from the 1993 eruption of Mt Aso, Japan have been used to determine the refractive indices from 1 to 20 μm. These preliminary measurements have spectral features similar to ash values that have been used to date, albeit with slightly different positions and strengths of the absorption bands. The refractive indices have been used to retrieve ash properties (plume height, optical depth and ash effective radius) from AATSR and SEVIRI instruments using two versions of Oxford-RAL Retrieval of Aerosol and Cloud (ORAC) algorithm. For AATSR a new ash cloud type was used in ORAC for the analysis of the plume from the 2011 Eyjafjallajökull eruption. For the first ~ 500 km of the plume ORAC gave values of plume height 2.5-6.5 km, optical depth 1-2.5 and effective radius 3-7 μm which are in agreement with other observations. A weakness of the algorithm occurs when underlying cloud invalidates the

assumption of a single cloud layer. This is rectified in a modified version of ORAC applied to SEVIRI measurements. In this case an extra model of a cloud underlying the ash plume was included in the range of applied models. In cases where the plume overlay cloud this new model worked well showing good agreement with correlative Cloud-Aerosol Lidar with Orthogonal Polarization (CALIOP) observations.

Volcanic plumes formed by explosive eruptions are mixtures of gas, quenched and fragmented silicate material (tephra) and other aerosol particles derived from both the magmatic emissions and background air (e.g. Mather et al.; 2003; Durant et al.; 2010; Ilyinskaya et al.; 2010; Oppenheimer et al.; 2010). The particles created during a volcanic event are classified according to size with the smaller solid particles (radii < 2 mm) referred to as volcanic ash (Schmid; 1981). The effects of airborne ash include:

Aviation: Volcanic ash is a hazard to aviation (Casadevall; 1994). Before March 2010 the Civil Aviation Authority did not permit civil aircraft to fly in the presence of volcanic ash. Following the 2010 Eyjafjallajökull eruption this zero-tolerance approach was changed to permit flights within ash concentrations less than 2×10^{-3} g cm^{-3} (CAA; 2010).

Climate: Injection of volcanic ash into the stratosphere and troposphere influences the Earth's radiation balance by interacting with both solar and thermal radiation as a function of the ash's optical properties (Solomon et al.; 2007). In the troposphere volcanic aerosols indirectly modify climate by acting as cloud condensation nuclei. This happens over the range of volcanic activity from quiescent degassing (Yuan et al.; 2011) to large volcanic eruption plumes.

Human Health: High levels of respirable ash (particle radius < 5 μm) in the air are not yet known to result in serious injury or disease from inhalation (Horwell and Baxter; 2006). However acute respiratory symptoms are commonly reported by people during and after ash falls (Blong; 1984).

Heavy ash fall may result in the collapse of roofs under the weight of ash and this can be deadly for people within buildings. The deposition of volcanic ash can increase trace metal (iron) concentrations in the local environment, especially following explosive eruptions (Martin et al.; 2009). If deposition occurs in the ocean, this can increase the productivity of phytoplankton in areas with limited nutrients (Jones and Gislason; 2008; Gabrielli et al.; 2008).

Changes in style of activity are common during eruptions, with explosive eruptions being particularly favoured by high (magmatic) gas content, and high melt viscosity (andesitic to rhyolitic magmas), or by the presence of external water (e.g. Sheridan and Wohletz; 1983; Scandone et al.; 2007). Component and morphological analyses of the erupted ash, and comparison of these data with those from other monitoring techniques, demonstrates a clear relationship between ash features and styles of explosive activity (e.g. Heiken and Wohletz; 1985; Martin et al.; 2008; Rust and Cashman; 2011; Taddeucci et al.; 2004).

Remotely sensed ash properties have the potential

- to warn of an aviation hazard,

- to act as the basis of a quantitative estimate of

  - ash fall out,
  - volcanic perturbation of the radiative field,
  - climate perturbations

- to investigate the interactions between ash and the biosphere (e.g. cloud seeding, ocean fertilization),

- to quantify volcanic process involved with ash generation and plume evolution.

Volcanic Cloud Properties

The characterization of a volcanic cloud can be broken into two scales:

- plume macrophysical properties, principally plume morphology which is usually simply described by plume altitude and thickness,

- plume microphysical properties which characterise the ash properties through quantities such as ash shape, size and composition.

Plume Height

For Plinian eruptions plume height is determined by the rate and intensity of the magma discharge, the density of erupted material and the temperature difference of the plume with the surrounding air (Sparks; 1986). The eruption column typically overshoots the height of neutral buoyancy and relaxes back to form a layer of material whose thickness is typically a few kilometres for a tropospheric eruption. Sparks et al. (1986) observed that cloud thickness is driven by the size of this overshoot; the ratio of umbrella cloud thickness to the maximum height of momentum driven ascent is typically 0.25 - 0.3. While atmospheric diffusion and sedimentation will tend to thicken the plume over time, the variation of wind with height can shear the plume into thin layers. For example lidar observations of plumes from the 2010 Eyjafjallajökull eruption gave layer thicknesses less than 1 km (Sicard et al.; 2011). Although models can calculate the dispersion of ash (Witham et al.; 2007) their accuracy depends critically on source parameters, in particular the eruption column height (Stohl et al.; 2011).

Ash Particle Size & Shape

Figure 1 shows an SEM image of volcanic ash collected from the 1993 eruption of Mt Aso, Japan. The ash particles cover a wide ranges of sizes and display shapes from the near spherical to highly complex angular shapes. In general, volcanic ash particle size distributions tend to be multimodal with the size, shape and composition being a function of the processes of formation. The majority of particles range from nanometres to millimetres in size (Heiken and Wohletz; 1985). The volcanic ash particles within a plume can include:

- volcanic glass formed from fragments of the molten part of magma that cooled and solidified during eruption,

- minerals or crystals that grow within the magma while it is below the earth's surface,

- rock fragments from the walls of the magma conduit,

- particles formed from the condensation of volcanic gases.

Hence the composition, grain-size and morphology of volcanic ash particles contains important information about the processes of magma ascent and fragmentation in volcanic eruptions (e.g. Heiken and Wohletz; 1985; Rust and Cashman; 2011). Further process alter the particle properties such as

- adsorption of species into the particle surface,

- fragmentation by the explosive expansion of volcanic gases,

- coagulation of particles,

- condensation of gases (e.g. water or sulphuric acid) to coat the particle,

- sedimentation.

The size and shape of ash particles is also critical in influencing the transport of ash through the atmosphere. In the absence of coagulation and vertical winds the process that determines the maximum life-time of a particle is sedimentation. Figure 2 shows the calculated fallout time for spherical particles as a function of particle size and initial height. It is suggested that the non-sphericity of ash particles further slows their fallout (Riley et al.; 2003). Given this caveat it is apparent that particles whose radii are greater than about 15 μm are removed from the plume within the first day following the eruption. Very fine ash (radii less than ~ 1 μm) is predicted to exist in the atmosphere for over a year but this is contradicted by observations that suggest very fine ash falls out faster than fluid dynamics predicts (Rose and Durant; 2009). Further work is required to understand this anomaly.

Preliminary Measurements of Ash Optical Properties

An irony of remote sensing is that often properties of the target need to be known to make full use of the remote measurement. In the case of gaseous species this is the molecular spectroscopy of the target gas. For aerosol or cloud, a priori information is needed on the complex refractive index, and to a lesser extent on the size and shape of the particles. For volcanic ash, a difficulty is that these assumed properties are likely to change during an eruption. The fewer a priori assumptions that are made about the target the lower is the chance of making spurious deductions caused by variations in a quantity assumed constant.

Existing measurements of volcanic ash refractive indices, as listed in Table 1, are extremely limited. There are a few more published refractive indices of volcanic material (e.g. basalt, Pollack et al.; 1973; Egan et al.; 1975; andesite Pollack et al.; 1973; Egan et al.; 1975; pumice, Volz; 1973; obsidian, Pollack et al.; 1973; granite, Toon et al.; 1977), these should in principle show similar spectral signatures to the ash. In order to exploit new instruments such as high resolution spectrometers, reference refractive indices are needed for a range of ashes and their mineral and rock components.

Transmission Measurements

Reported here are preliminary refractive indices derived from transmission spectra of resuspended volcanic ash. Figure 3 outlines the basic configuration of the experiments undertaken. A sample of ash from the 1993 eruption of Mt Aso was collected from a bomb shelter where 1 to 2 m of ash had accumulated. Data on the composition of the ash will be addressed in future studies. For context, the composition of the 1989 Aso eruption scoria is reported by Ono et al. (1995) as SiO_2=54.71 wt%, Na_2O=3.01 wt%, K_2O=2.00 wt%. The ash sample was sieved to < 22.5 μm and this fraction was resuspended and introduced into an aerosol test cell. The aerosol cell has optical windows fitted, allowing the aerosol absorption to be measured via a Fourier Transform Spectrometer, FTS. The aerosol size distribution was determined using techniques insensitive to particle refractive index and the aerosol vented into a fume cupboard.

All of the measurements were undertaken at the Molecular Spectroscopy Facility at the Rutherford Appleton Laboratory. The aerosol cell used had an optical path length of 26 cm. Spectral intensity measurements were made using a Bruker IFS-66 FTS. Measurements of the detected spectrum were ob-

tained with and without the aerosol to calculate the transmission spectrum, $T(\lambda)$. A correction was made to the transmission spectrum to remove water and carbon-dioxide gas absorption lines; this was achieved via a separate retrieval of these gas species' concentrations.

Data Analysis and Results

The refractive indices were determined from the transmission spectrum. Aerosol cell transmission relates to the physical properties of the aerosol via Bouguer's Law

$$T(\lambda) = e^{-\beta^{\text{ext}}(\lambda)x}, \qquad (1)$$

where $T(\lambda)$ is the transmission, β^{ext} the volume extinction coefficient at wavelength λ, and x the path length though the test cell. Assuming a particle scattering model (Mie theory or T-matrix to deal with non-spherical particles) and knowing the particle size distribution allows the extinction coefficient to be calculated from

$$\beta^{\text{ext}} = \int_0^\infty Q^{\text{ext}}(r, m(\lambda), \lambda)\pi r^2 n(r)\, dr, \qquad (2)$$

where Q^{ext} is the extinction efficiency, r is the particle radius, m the complex refractive index and $n(r)dr$ is the number of particles with radii between r and $r + dr$.

The complex refractive index wavelength dependence $m(\lambda)$ is represented by a damped harmonic oscillator model to reduce the number of model parameters to less than the number of measured spectral points. Optimal estimation is then used to derive the band model parameters (and hence refractive index) and aerosol size distribution. The method has been described in detail by Thomas et al. (2005).

The derived refractive index of Aso ash is shown in Figure 4. The refractive index is dominated by a broad absorption band situated at about 9.5 μm which can be associated with the stretching vibration of Si-O. The much weaker and narrower band at about 3 μm is probably from O-H stretch. These are preliminary results, data at wavelengths shorter than 1 μm (not plotted) are a forward model extrapolation and should be used with caution.

Identifying Volcanic Ash

A volcanic plume perturbs the Earth's radiation field by scattering and absorbing radiation and by emitting radiation in the infrared. In the shortwave the particle size and refractive index means a volcanic plume resembles cloud

from which it may only be distinguishable by the cloud's morphology. The infrared (IR) transmission or emission spectra of volcanic plumes show a rapid variation with wavelength due to absorption lines from atmospheric and volcanic gases, as well as broad-scale features principally due to particulate absorption or emission. While the gas lines have provided important insights into volcanic processes (Burton et al.; 2001, 2003; Oppenheimer et al.; 2006; Edmonds et al.; 2003; Sawyer et al.; 2008) the ash features have not been analysed to the same extent. In the infrared, ash is detectable by its distinctive emission spectra. This is shown in Figure 5 where the similar amounts of material of the same size are shown to have distinct emission spectra. The spectra are presented in terms of optical depth τ defined for a plume of thickness L as

$$\tau = \int_0^L \beta^{\text{ext}} \, dz, \tag{3}$$

while the ash size distribution is characterised by the effective radius r_{e} defined by

$$r_{\text{e}} = \frac{\int_0^\infty r^3 \, n(r) dr}{\int_0^\infty r^2 \, n(r) dr}. \tag{4}$$

Volcanic aerosol is assumed to conform to a log-normal distribution described by

$$n(r) = \frac{N_0}{\sqrt{2\pi}} \frac{1}{\ln(S)} \frac{1}{r} \exp\left[-\frac{(\ln r - \ln r_{\text{m}})^2}{2 \ln^2(S)} \right], \tag{5}$$

where N_0 is the total particle number density, r_{m} is the median of the size distribution and S is a parameter than controls the spread of the size distribution. For a log-normal distribution r_{m} and r_{e} are related by

$$r_{\text{e}} = r_m \exp\left(\frac{5}{2} \ln^2 S \right).$$

Figure 5 shows that between about 10 and 12 μm the optical thickness of ash and sulphuric acid decreases whereas water or ice increases. Measurement channels centred near 11 and 12 μm are common on meteorological imaging instruments and have been widely exploited to study volcanic ash clouds. Examples are listed in Table 2. These instruments generally report brightness temperatures T_{11}, T_{12} at these two wavelengths rather than a radiance. The magnitude of the brightness temperature difference has been shown to be a function of the ash size (Prata; 1989a; Wen and Rose; 1994).

While a powerful and useful tool, there are cases where the technique is not robust (Prata et al.; 2001). They include:

9

1. Strong temperature inversions near the surface, which can result in a negative T_{11} - T_{12} in clear sky conditions.

2. Dry soil, e.g. deserts or wind blown dust, is also often characterised by a negative T_{11} - T_{12}, for the same reasons as volcanic ash.

3. Cloud tops which overshoot the tropopause can also show a negative T_{11} - T_{12} due to the inversion of the temperature gradient in the stratosphere.

4. Very thick volcanic ash, ash mixed with ice (quite a common occurrence, since volcanoes generally emit large quantities of water vapour), or ash which lies below an airmass with a high water vapour content.

5. Instrument noise or collocation errors between the 11 and 12 μm channels.

Use of a 3.7 μm channel and information from shortwave channels can alleviate this problem (Ellrod et al.; 2003) as their dependence on the properties of volcanic ash differ from the $8-12$ μm region.

The ash signature depends on the composition and size distribution of ash particles. Figure 6 shows an example of different optical depths computed using the same size-distribution (with an effective radius of 2 μm) and different refractive indices. The published infrared spectral refractive indices of volcano-related ash and rock show a large variability, presumably because of changes in the ash composition. This is reflected in the variability of infrared spectra measured from satellites for different volcanoes and eruptions (Clarisse et al.; 2010; Gangale et al.; 2010).

Other Volcanic Products

In addition to ash volcanic eruption can release large quantities of gas, the principle being H_2O, CO_2, CO, SO_2, H_2S, HCl. Of these SO_2 has been observed from space (e.g. Read et al.; 1993; Walker et al.; 2012) and its evolution tracked remotely. While there are several observations of ash and SO_2 being collocated this is not always true. The most famous example being the El Chichón 1982 eruption when the ash and SO_2 cloud were observed to be spatially separated (Seftor et al.; 1997). Other examples include Hekla 2000 eruption (Rose et al.; 2003) and the Eyjafjallajökull eruption of 2010 (Thomas and Prata; 2011). The reason being that the SO_2 and ash had different altitudes of neutral buoyancy within the eruption column and as a result were separated by wind shear. Hence while SO_2 may indicate the presence of ash it should not be used as a proxy for ash.

Remote Sensing of Volcanic Plume and Ash Properties

There are three distinct time regimes for remote sensing of volcanic ash.

- The identification of volcanic ash for hazard avoidance. In this case a fast (real time) algorithm is needed that recognises ash with a low (less than once per year) false detection rate.

- The characterisation of volcanic plume properties (e.g. altitude, erupted mass) in near real time for

  - plume model initialisation and validation
  - and to help quantify the immediate impact of ash on the biosphere.

- A full and detailed characterisation of volcanic ash properties to help understand volcanic processes (both in the plume and potentially within the volcano itself).

Over twenty different satellite instruments have been used to measure volcanogenic gases and/or particles. Earlier work is well summarised in Oppenheimer (1998) and Francis and Rothery (2000) while Thomas and Watson (2010) provide information on more recent missions. Here we concentrate on three instruments which have been relatively underexploited for volcanological studies.

MIPAS

The Michelson Interferometer for Passive Atmospheric Sounding (MIPAS) is a limb viewing Fourier transform spectrometer measuring from 685 cm^{-1} to 2410 cm^{-1} at a spectral resolution of 0.025 cm^{-1}. MIPAS was launched in March 2002 on the European Space Agency's Environmental Satellite (EN-VISAT). The ENVISAT spacecraft is in an 800 km sun-synchronous polar orbit with a nominal repeat period of 35 days. In March 2004, MIPAS began experiencing irregular motion of the scanning mirrors. To rectify this problem, the path length over which the mirrors moved was decreased, reducing the resolution of the spectra to 0.0625 cm^{-1}. The reduced resolution nominal scan pattern consists of 27 observations of the Earth's limb with 1.5 km spacing in the lower atmosphere. A complete scanning profile, then, takes about 65 s, resulting in over 1000 scans taken daily. There is nominally 330 km horizontally between the first (highest) and last (lowest) sweeps in

a scan with along-track horizontal spacing between scans of 410 km. The field-of-view is about 3 km vertically and 30 km horizontally.

Although MIPAS has been used extensively to determine atmospheric trace gas properties (e.g. Burgess et al.; 2006; Payne et al.; 2007) and to observe clouds (e.g. Spang et al.; 2005; Hurley et al.; 2011), to date there have been no reports of MIPAS observations of volcanic ash.

Recognition of volcanic ash using singular vector decomposition of MIPAS spectra.

The Oxford MIPAS retrieval of clouds (Hurley et al.; 2011) uses the continuum radiance from a narrow band of wavenumber ranges between 930 and 965 cm^{-1} to retrieve a cloud effective fraction (CEF) defined as the fraction of the field-of-view that is covered by optically thick cloud. This is used to find the highest MIPAS scan altitude at which cloud is present. The cloud top height, cloud extinction and cloud top temperature are retrieved using the CEF and the continuum radiances from the scan above, at, and below the field-of-view at which the cloud top is found. However this approach does not determine cloud type. Extinction, cloud height, and cloud top temperature are retrieved, but any significant particulate plume can also show up in the retrievals, since the process identifies cases where the field-of-view is not clear. The retrieval of volcanic plumes is not a problem per se. These do have legitimate height, extinction and temperature, but it is useful to know when the cloud is composed of volcanic ash, as opposed to water or ice.

Plumes can be flagged roughly by inspecting the ratio of radiances from different areas of the MIPAS continuum. For ash it was found that an appropriate flag was:

$$\frac{R_{(800-830 \text{ cm}^{-1})}}{R_{(935-960 \text{ cm}^{-1})}} \quad < \quad 1.3, \tag{6}$$

where R is the mean continuum radiance between the lower and upper bounds of the wavenumbers indicated in the subscripts. The flag correctly identified many areas where the volcanic output from Puyehue and Nabro was observable in MIPAS measurements. This flag is particularly good at picking out strong signals, but in areas with less clear ash loadings, the method will not work.

Using singular vector decomposition (SVD), it is possible to identify plumes more definitely, picking up weaker signals, and signals which also include regular clouds. A similar approach to that used by Hurley et al. (2009) is adopted (although in that case, singular vectors were obtained for a set of

calculated radiances, not measured atmospheric spectra). First, before a volcano has erupted, several days of MIPAS data at the volcano's latitude and a range of nominal altitudes are taken as a "clean atmosphere training set" for atmosphere not containing a volcanic plume. Singular vectors, $\mathbf{v}_i$, are fitted using the method given by Press et al. (1992). These vectors represent the orthogonal components of the given spectra, so that any of the training set spectral measurements, R, can be exactly reproduced by a weighted sum of the singular vectors, obtained through a least squares fit:

$$\mathbf{R} = \sum_i \lambda_i \mathbf{v}_i, \tag{7}$$

where λ_i is the weight of the ith singular vector. Since the training set is expected to contain clear sky, and cloudy sky data, it can be used to fit measurements after the eruption where volcanic signals are not present. There are as many singular vectors as original measurements used in the training set, but the principal modes of variation are found only in the first few terms. It is therefore appropriate to truncate the sum given in Equation 7 after a few terms. In this case, the first nine singular vectors were found to contain 90 % of the variability between different measured spectra in the training set.

For post-volcanic measurements, the flag defined by Equation 6 is used to provide cases where there is a strong volcanic signal. The original singular vectors are fitted to these new measurements, and the residual is that part of the spectrum that cannot be explained by our prior vectors for clean sky (and is therefore assumed to contain a volcanic signature). From several days of data, these residuals are collected, and used to obtain a new set of singular vectors which contain the principal orthogonal signals for volcanic plumes. The volcanic singular vector is specific to the fitted ensemble as it contains information about aerosol composition which may vary during an eruption and between different volcanic events.

Figure 7 shows an example of fitting the calculated singular vectors to real data. The values of λ_i for the first two "clean" singular vectors and the first volcanic singular vector are shown. Note the much greater magnitude of the first two panels, which capture the strongest modes of variability for the clean signal, the diurnal cycle, and the presence of cloud. The first volcanic singular vector, shown in the bottom panel, has almost no concentration before the eruption, but sporadically shows up post-eruption. Arrows show where the original volcanic flag has been triggered. The new method identifies more scans that include ash than found using the continuum flag.

AATSR

The Advanced Along Track Scanning Radiometer (AATSR) is the current operational instrument in a series of nadir viewing radiometers (ATSR-1, ATSR-2 and AATSR commonly referenced as ATSR). AATSR, like MIPAS, is part of the payload on ENVISAT. A feature of the ATSR instruments is that they provide two views of the same scene within $\sim$90 s of each other, the first centred on a viewing zenith angle of 55°, the second at nadir. The parallax between the two views allows for the determination of the altitude of features by purely geometric means. For AATSR each view is made in seven spectral channels centred at 0.56, 0.66, 0.86, 1.6, 3.7, 11 and 12 μm and reported as sun-normalised reflectances in the shortwave (i.e. $R_{0.56}$, $R_{0.66}$, $R_{0.86}$, $R_{1.6}$) and brightness temperatures in the infrared (i.e. $T_{3.7}$, T_{11}, T_{12}). As a polar orbiting instrument, it provides a single day-time and single night-time overpass at approximately 10:30 am/pm local time. The instrument swath width of 512 km (with a 1 km pixel size) means that it takes the instrument three days to provide near-global coverage. Thus, for a given eruption, AATSR will only be able to provide a measurement of the proximal plume once every three days.

Previous volcanological work using the ATSR series has included the thermal monitoring of volcanic hotspots (e.g. Wooster and Rothery; 1997). Prata and Grant (2001) determined ash properties from the 11 and 12 μm brightness temperatures in addition to plume height determined from the parallax formed between the ATSR forward and nadir views. Here, the AATSR instrument is used to produce volcanic cloud products from two independent methods:

1. The stereo matching approach is used to produce an estimate of geometric ash cloud top height.

2. The brightness temperatures, in conjunction with knowledge of the vertical temperature structure of the atmosphere, is used to determine ash cloud height using the shortwave channels to constrain the optical depth and microphysical properties of the cloud.

Identifying Ash in AATSR Imagery

The identification of ash in imager data has traditionally relied upon the brightness temperature difference between 11 and 12 μm channels. In daylight scenes, the shortwave channels can also provide additional constraints - ash will typically have a low albedo compared to cloud and is also more absorbing in the green than the red. These features have been combined to

produce an AATSR volcanic ash flag, which uses thresholds on the following quantities:

- T_{11} - T_{12}

- T_{11} - $T_{3.7}$

- $R_{0.67}$

- The Normalised Difference Vegetation Index (NDVI), defined as

$$\text{NDVI} \;=\; \frac{R_{0.55} - R_{0.67}}{R_{0.55} + R_{0.67}} \tag{8}$$

Lean (2009) provides a test specifically for AATSR in daylight conditions whereby a pixel which meets all four of the following conditions:

$$
\begin{aligned}
T_{11} - T_{12} &< -0.1 \\
T_{11} - T_{3.7} &< -20 \\
R_{0.67} &< 0.1 \\
\text{NDVI} &< 0.1
\end{aligned}
\tag{9}
$$

is deemed to be ash. For night time scenes, the solar reflectance proportion of the 3.7 μm signal drops to zero, as do the shortwave channels, and the test becomes:

$$
\begin{aligned}
T_{11} - T_{12} &< -0.1 \\
T_{11} - T_{3.7} &< 0
\end{aligned}
\tag{10}
$$

Using these tests, AATSR data can be rapidly checked for evidence of volcanic ash. As these thresholds are instrument and calibration dependent further research would be needed for their use on other ATSR instruments.

Stereo Ash Plume Height Retrieval Algorithm (SAPHRA)

The SAPHRA algorithm consists of two stages:

1. The detection of possible volcanic ash plumes, based on the test specified in Equations 9 during the day and Equations 10 at night.

2. The estimation of the height of detected plumes using stereo-matching of the forward and nadir brightness temperature difference images.

Stereo matching is a well established tool for the determination of cloud and plume heights, both from ATSR instruments (Muller et al.; 2007; Prata and Grant; 2001) and NASA's Multi-angle Imaging Spectro-Radiometer (MISR) on board the Terra satellite (Moroney et al.; 2002). The method employed here is the simplest approach to the problem of matching features in the two views:

1. $T_{11} - T_{12}$ is calculated for the entire scene in which ash has been detected, in both views.

2. The correlation between the two brightness temperature difference images is calculated using a sliding window of $n \times n$ pixels; where n is ~ 3.

3. The images are offset by one pixel in the along-track direction, and step two is repeated.

4. Step three is repeated twenty times, creating correlation images of the two brightness temperature difference fields for offsets of 0 - 20 pixels.

5. The offset for maximum correlation is determined for each pixel, and converted to a geometric altitude.

The use of $T_{11} - T_{12}$ ensures that the ash plume has a strong contrast to the rest of the image, and gives a large change in correlation as the two views are aligned. Under the naive assumption that the uncertainty in the retrieved height is entirely due to the alignment, a one pixel error implies an altitude uncertainty of approximately 1.4 km. Other geometric cloud/plume height retrievals often use more complex pattern matching algorithms to produce a height map, such as the Multi-point Matchers M2, M3 (Muller et al.; 2002) and M4 (Muller et al.; 2007), which could be investigated for use here. However, as we are interested solely in a clearly defined plume, the correlation method is sufficient for evaluating our approach.

SEVIRI

The Spinning Enhanced Visible and Infrared Imager (SEVIRI) is a scanning radiometer on-board the operational Meteosat Second Generation weather satellite which is in a geostationary orbit nominally located on the Greenwich meridian. SEVIRI provides image data of the Earth in eleven narrow band channels centred at 0.635, 0.81, 1.64, 3.92, 6.25, 7.35, 8.70, 9.66, 10.8, 12.0 and 13.4 μm. A key feature of this instrument is its continuous imaging with a baseline repeat cycle of 15 min. The imaging sampling distance is 3 km at the sub-satellite point. SEVIRI has been used to identify volcanic hotspots (Wooster et al.; 2000) as wells as to study lava flows at erupting volcanoes (Hirn et al.; 2009). Ash and SO_2 have also been measured using the five channels centred at 6.25, 7.35, 8.70, 10.8, 12.0 (Prata and Kerkmann; 2007). More recently Stohl et al. (2011) used SEVIRI estimates of ash mass loading to infer the ash emission from the Eyjafjallajökull 2010 eruption as a function of time and altitude.

ORAC retrieval of ash plume height and physical properties

The Oxford-RAL Retrieval of Aerosol and Cloud (ORAC) algorithm is an optimal estimation (OE) retrieval scheme designed to provide estimates of aerosol optical depth and effective radius, cloud top pressure, height and temperature, cloud particle effective radius, cloud optical depth and cloud type (generally liquid water or ice) from multispectral imagery. The scheme has been used to produce a cloud product from the full ATSR-2 and AATSR record up to 2010 (Poulsen et al.; 2011; Sayer et al.; 2011). The ORAC cloud scheme has been modified to determine ash cloud properties by using a radiative forward model based on ash particles described by a lognormal distribution (the lognormal spread is fixed at 1.77 but the effective radius is allowed to vary in range 0.01 - 10 μm) and the Aso refractive indices described in Section 3. This principally involves creating lookup tables describing reflectance and transmission of the ash plume for a range of solar and satellite geometries.

Assuming the plume is homogeneous, the integral in Equation 3 can be completed and so the plume thickness, L, and optical depth τ are related by

$$\tau = \beta^{\mathrm{ext}} L \tag{11}$$

The ash loading m [usually in g per m^3] can be calculated from

$$m = \underbrace{\rho \int_0^\infty \frac{4}{3}\pi r^3 n(r)\, dr}_{\text{mass per unit volume}} \times \underbrace{\frac{\tau}{\beta^{\mathrm{ext}}}}_{\text{L}} = \frac{4\pi r_{\mathrm{e}}\rho\tau \int_0^\infty r^3 n(r)\, dr}{3\beta^{\mathrm{ext}}} \tag{12}$$

where ρ is the density of the ash (Wen and Rose; 1994). If the particle size-distribution is assumed to be log-normal the column loading becomes

$$m = \frac{4}{3}\frac{\rho\tau}{\bar{\sigma}^{\mathrm{ext}}}\pi r_{\mathrm{e}}^3 \exp\left(2\ln^2 S\right) \tag{13}$$

where $\bar{\sigma}^{\mathrm{ext}}$ is the average extinction cross-section per particle given by

$$\bar{\sigma}^{\mathrm{ext}} = \frac{\beta^{\mathrm{ext}}}{N_0} \tag{14}$$

CAA restrictions on aircraft flights are in terms of the density of ash rather than the column amount. There are three approaches to estimate this quantity from the mass loading:

1. Use a correlative measurement of the plume thickness, L, e.g. from lidar, then estimate the mass density through

$$\rho = \frac{m}{L} \tag{15}$$

17

2. Assume a typical volume extinction coefficient to convert a plume's optical depth into physical depth.

3. Assume the plume thickness is the same as its altitude. This then provides a minimum possible mass density under the assumption the plume is homogeneous.

It is worth noting that the simultaneous retrieval of all state parameters provided by the OE method ensures that a physically consistent and numerically optimal estimate of the state is produced. It is clear that, although thermal IR channels mostly provide information on the cloud top pressure, height and temperature, the transmission and emission values of the cloud will depend on the optical depth and effective radius, which are mostly determined from the shortwave channels. Conversely, the above and below cloud transmissions in the shortwave will be weakly (if we assume the channels used are atmospheric window channels) dependant on the cloud height. Due to the large differences in the optical properties of ash, water droplets and ice crystals, ORAC has been proved to provide an effective way of detecting ash in satellite imagery; ash clouds cannot be well fit using either water or ice cloud properties and vice versa.

Here we will demonstrate an ability to determine ash properties when a plume is located above a cloud. This is particularly useful as there were many instances of ash overlying cloud during the Eyjafjallajökull, 2010 and Grimsvötn, 2011 eruptions.

In summary, quantifying a volcanic cloud requires knowledge of ash loading, composition, morphology and size, as well as the physical dimensions and location of the ash plume. In addition, tephra from explosive volcanic eruptions holds information about magma dynamics in the critical zone where fragmentation occurs and eruption style is decided. In this work new algorithms are presented that determine plume and ash properties based on preliminary laboratory measurements of ash optical properties.

Case Study I: The 2011 Puyehue-Cordón Caulle Eruption

The Puyehue-Cordón Caulle volcanic complex (Singer et al.; 2008) forms part of the Andes and is located in Puyehue National Park, Chile. The eruption began in June and continued through the remaining months of 2011. A summary of the first two months of activity is summarised below.

From 27th April, seismic activity was detected. The frequency of earthquakes increased on 2nd June and was followed, on 4th June, by an explosion

from Puyehue-Cordón Caulle that produced a plume of ash and gas, rising to an altitude of 12.2 km above sea level (asl) as noted by Observatorio Volcanologico de los Andes del Sur (OVDAS)(Chile) (2011) and Servicio Nacional de Geologia y Mineria scientists (Servicio Nacional de Geologia y Mineria; 2011a,b,c,d). Initially, plumes drifted south at 5 km asl and drifted west and east at an altitude of about 10 km.

From the 4th June and on the following days the ash plumes were generally transported in the SE to NE sector. The Buenos Aires VAAC reported that on 4th June ash plumes rose to altitudes of 10.7-13.7 km and drifted 870 km ESE (Global Volcanism Program; 2011a). On the 5th June, the ash plume was estimated to be between 10.7-12.2 km located 1,700 km ESE of the volcano over Atlantic Ocean. On 6th June, a new part of the plume was located 170 km ENE of the mountain, while the previous part of the plume continued to be transported ESE over the ocean. On the 7th June the ash plume was reported at heights of 5.5-9.8 km (Global Volcanism Program; 2011a). Volcanic activity continued over the following days, leading to the cancellation of several flights in Argentina, Uruguay and Brazil. By 12th June, the ash plume had reached Australia, and New Zealand. On 13th June, a MODIS image showed a large volcanic ash plume over Argentina which was reported to lie between 4 and 8 km (NASA Earth Observatory; 2011). From 22 June to 5th July, the eruption continued with less activity and lower plume heights in the range 2 and 4 km (Global Volcanism Program; 2011a).

On 7-8th July an increase in the plume height led to the cancellation of flights in Argentina and Uruguay (France-Presse; 2011). During the following few days the plume altitude decreased and was reported to be 3 km (9th July) l, 2 km (17th July) and 5 km above the crater on the 18th July. Between 25 July-1 August, the eruption continued with plumes rising 2-5 km above the crater. Eruptive processes continued through the remaining months of 2011(Global Volcanism Program; 2011a).

Using AATSR to Identify the 2011 Puyehue-Cordón Caulle Ash Cloud Height

SAPHRA has been used to identify the height of the ash plume from the 2011 Puyehue-Cordn Caulle eruption as viewed by AATSR on the 6th of June. Figure 16 shows an image generated from red, green and blue channels of the MEdium Resolution Imaging Spectrometer (MERIS) which is on board the Envisat platform with AATSR. Superimposed on the MERIS image is a visible-near infrared false colour image from AATSR. The primary ash plume

is very clear, and its altitude can be estimated from the shadow it casts on the surface as 12.7 ± 1.8 km (the solar elevation at the time the satellite over-passed the plume was about 20°). A less distinct, lower altitude ash cloud can also be made out to the south of the main plume, particularly in the AATSR image.

Figure 8a shows the results of applying the ash flag to both views of the AATSR instrument. Both ash plumes are successfully detected in both views of the instrument. The greater sensitivity of the forward view, due to its greater atmospheric path-length, results in a larger number of ash pixels, including some possible false detections along the southern edge of the image, being detected in this view; but the two views generally produce very consistent results. The parallax between the two views is also very clear in this image, particularly along the northern edge of the main plume.

The results of the stereo matching technique, using a 3×3 pixel sliding window, are given in Figure 8(b). Heights retrieved in the main plume are typically around 12 km, while the lower ash cloud to the south has produced a height of approximately 5 km. There is also evidence that there is some decrease in the main plume height from the west to the east of the image.

Figure 9 shows a histogram of the heights from Figure 8(b), as well as two Gaussians which have been fitted to the two peaks apparent in the figure. Under the assumption that the heights of both distinct plumes in the scene are constant throughout the image, the plume heights can be characterised as 11.9 ± 1.4 km for the main plume and 5.2 ± 2.5 km for the cloud to the south.

The variability in the retrieved height of the lower ash plume is greater than might be expected from alignment error alone. The stereo matching method has several limitations related both to the measurements provided by the instrument and the assumption that the two images of the plume will match when the parallax is removed. These uncertainties can be summarised as follows:

- As the two views of ATSR are obtained at very different viewing geometries, they will see different parts of the plume and any surrounding clouds, as well as shadows cast by both the plume and clouds.

- The native pixel size in the forward view of ATSR is approximately twice the size of that in the nadir view. Although Level 1b data from the instrument has both views interpolated onto a common grid, this resolution difference produces noticeable differences in the clarity of features in the two views.

- There can be expected to be some evolution in the scene over the 90 s

gap between the forward and nadir scans of the instrument; however, for most scenes this will be insignificant on the 1 km spatial scale of an instrument pixel.

- Stereo matching will be most successful for images with strong features that lie perpendicular to the satellite track, as they will provide clear markers of parallax. Thus, for the greater part of an ATSR orbit, plumes which extend in an east-west direction will be better retrieved.

- ATSR have a collocation error of typically one pixel (although often more) between the forward and nadir views. Thus, features at sea level will often not coincide in the two images. This error is probably the most serious of those listed here, as it can result in a consistent bias in the retrieved height of up to a few kilometres. However, it is possible to correct for: in the results presented here, surface features have been used to align the two views by eye before applying the height retrieval algorithm. There is also an on-going effort to produce a global correction for the entire ATSR-2 and AATSR time series, which should solve this problem.

All of these limitations can contribute to an uncertainty which is significantly greater than the circa ±1.4 km error that results from the 1 km resolution of AATSR, especially for diffuse ash clouds. However, for a well defined, favourably aligned plume, such as the main plume in this case study, the variability in the retrieved plume height shows very good agreement with the expected error.

Using MIPAS to Identify the 2011 Puyehue-Cordón Caulle Ash Cloud

Figure 11 shows the first volcanic singular vector calculated using flagged spectra that were thought to contain the plume from the Puyehue eruption, viewed at an altitude of 12 km. The positive slope through the centre of the A-band is a well known feature to be expected, since it agrees with the empirical flag that was used to mark volcanic profiles. The SVD can be re-calculated at later times after the eruption in order to see the evolution of the plume's optical properties.

The geographical coverage of the plume can be inferred by looking for areas where the least squares fit of the singular vectors to a MIPAS spectra requires a significant contribution from the first volcanic singular vector i.e. $\lambda_{\text{volc},1}$. In these areas, the "clean" singular vectors could not satisfactorily represent the scene. Care must be used in interpreting these areas as no effort

has been made to account for unobserved portions of the plume. These occur through MIPAS's limited spatial sampling, by the plume being obscured by water or ice cloud or by the plume occurring below MIPAS's minimum sampling altitude.

Plotting the area of plume coverage over the next few months, it is seen that starting from a small localised area around the site of the volcano, the plume spreads out, reaching a peak in coverage around 30 days after the eruption, before rapidly dropping off. Figure 12a shows the southern hemisphere the day after the eruption has begun. A signal can be seen at the emission location of the volcano (marked with a triangle), as well as a further plume, to the east, which is from a later overpass of the satellite. Figure 12b shows the much increased coverage, but weaker signal strength of the volcanic signature a month later.

Over the course of the next two months, similar plots (not shown) show the coverage of the plumes increasing while travelling around the globe from west to east. Figure 13 shows fractional coverage between 60° S and 20° S for this time. Singular vectors calculated at the start of the eruption were just as effective at observing the plume vectors calculated a month later, suggesting that the plume did not significantly change in composition over the course of its lifetime. The reported altitudes of the ash plumes during June 2011 are generally in agreement with the MIPAS flagged locations of the plume. For example the peak plume altitude on June 6th was the 12 ± 1.5 km range, which is in agreement with both the reported observations and the AATSR stereo height retrieval. Plumes from later periods of the eruption were not observed as they did not reach high enough altitudes.

Case Study II: The 2011 Nabro Eruption

Nabro is a stratovolcano 2218 m high, located in the Afar depression in Eritrea, close to the border with Ethiopia (Wiart and Oppenheimer; 2005). There are no ground measurements for this volcano and it is an example of the importance of volcanic monitoring using satellite remote sensing. The seismic activity started in the evening of the 12 June 2011 with a magnitude 5.1 earthquake and continued for several hours (USGS Earthquake Hazards Program; 2011). The first satellite image with a discernible volcanic plume is the SEVIRI false colour image of 21:00 UTC of 12 June (EUMETSAT; 2011). In subsequent imagery the plume drifts to the NW so that by the evening of 13 June the plume is over Egypt. On 14 June an ash cloud was reported over southern Israel (The Jerusalem Post; 2011) which is consistent with satellite observations of SO_2. Volcanic plumes were reported at altitudes

of 9.1-13.7 km on 13th 6.1-10.7 km on 14th and 6.1-7.9 km during 15-20 June (Global Volcanism Program; 2011b).

On 15-16 June satellite measurements of SO_2 by the Infrared Atmospheric Sounding Interferometer (IASI) show an plume located over central Asia. The IASI measurements show two distinct filaments of SO_2 over Asia, (one at 10 km altitude and one at 15 km). The SO_2 plume reached the east coast of China on 18th June. During 22-26 June large amounts of sulphur dioxide continued to be detected by satellite sensors. The Toulouse VAAC reported that during 26-27 June plumes rose to altitudes up to 6.1 km. The satellite images show that the SO_2 signal gradually decreasing up to 28 June. The last ash plumes from this eruption were reported on 16 July (at an altitude less than 5.5 km) and on 17 July (Global Volcanism Program; 2011b).

Using MIPAS to Identify the 2011 Nabro Ash Cloud

Since different eruptions produce varied particles, the singular vector signatures have large differences. Within the AB and B bands, Figure 15 shows that the Nabro signature appears to contain the SO_2 ν_1 and ν_2 absorption bands which are centred at 1152 cm^{-1} and 1362 cm^{-1} respectively (this is not clearly visible in the Puyehue vector). This result can give us confidence that the technique is working. Preliminary retrievals of IASI data show that SO_2 emissions from Nabro are around an order of magnitude greater than those from Puyehue.

Figure 15 shows change in the spatial distribution of the plume over the course of the next six weeks. Starting from a localised zone, the area taken up fills much of the Northern hemisphere, but, as one would expect, weakens in signal strength.

Figure 16 shows the spatial coverage of the plume as a function of the volcanic singular vector calculated at different dates. The singular vector found at the start of the eruption (but fitted through the entire time period) reaches a maximum about 40 days after the start of the eruption before decaying. The singular vector found at the end of the eruption (also fitted through the entire time period) steadily increases with time. This is consistent with the ash and SO_2 (represented by the initial singular vector) dispersing, the ash precipitating and the SO_2 converting into sulphate aerosol. The final singular vector is consistent with the sulphate aerosol concentrations increasing following the oxidation of sulphur containing volcanic gases into sulphuric acid. Further work is needed to turn this qualitative interpretation of the MIPAS observation into quantitative estimates of aerosol concentration, composition and conversion rates.

Case Study III: The April - May 2010 Eyjafjallajökull Eruption

The Eyjafjallajökull is a stratovolcano, located close to Iceland's southern coast (Sigmundsson et al.; 2010). As reported by Global Volcanism Program (2011c), after an initial eruptive phase (from 20 March 2010) of lava flow but no significant ash and SO_2 emission, an explosive eruptive phase of the Eyjafjallajökull volcano began on the 14 April 2010. This was anticipated by a series of earthquakes in the night between 13 and 14 April. Following Zehner (2012), the explosive part of this eruption can be divided into three phases:

Phase I: 14 - 18 April

A phreatomagmatic eruption phase, ice and water from the ice cup above the caldera are directly in contact with the fresh magma in the vent. This produce a faster cooling of the ejected magma and large amount of ash injected in the atmosphere, as well as steams plumes. During this period the injection altitude of the plume was estimated between 2 and 10 km height (Marzano et al.; 2011; Stohl et al.; 2011) and the wind conditions transported the ash plume in a SE direction, toward Europe.

Phase II : 18 April - 4 May

From the evening of 18 April there was a magmatic eruption phase; water and ice from the glacier were not inside the vent. The intensity of the eruption was one order of magnitude lower than phase I, and there was a reduction in the amount of ash injected into the atmosphere. The altitude of the eruption column was between 2 and 5 km (Zehner; 2012; Stohl et al.; 2011).

Phase III: 5 May - 24 May

Between 3-5 May an increase in seismic activity was reported followed by a more intense explosive phase of the eruption. Ash production increased and the eruption column altitude was reported between 4 and 10 km (Stohl et al.; 2011). In this period ash plumes were transported over Europe and the Atlantic ocean.

The volcanic plumes from the eruption of Eyjafjallajökull starting in April 2010 resulted in the cancellation of 100,000 flights over Europe affecting roughly 10 million passengers (European Commission; 2010). The airline

industry lost an estimated £153 million a day during the 15-21 April 2010 period when European airspace was closed (Mazzocchi et al.; 2010).

ORAC-AATSR Retrieval of the 2010 Eyjafjallajökull Ash Plume

The Eyjafjallajökull eruption plume is highlighted in the AATSR-based false colour image shown in Figure 17a. The plume is clearly visible and can be seen to extend over cloud free land and ocean, as well as over low-lying cloud as it bends from a east-west alignment to a southerly direction. There are also several relatively small convective clouds which appear to be coincide with the ash plume in this region. The ORAC retrieval scheme has been applied to this image, using volcanic ash optical properties in addition to the standard water and ice cloud types. Figure 17b shows the best fitting cloud type for each retrieved pixel in this scene for which

- a priori surface reflectance data were available (the MODIS surface BRDF product was not available for much of Iceland, unfortunately including the region under the ash plume),

- the retrieval converged, producing an optical depth of greater than 0.2,

- the cloud top height was greater than zero.

No cloud mask was applied to the scene before the retrieval was run, so the later two tests are needed to remove clear-sky pixels.

The ash plume is readily apparent, but it is also clear that ash has produced the best fit in regions where we would not expect any ash to be present. This is a product of the under-constrained nature of the retrieval problem - in some cases where the forward model is not a good representation of the real world (multi-layer cloud, cloud edges, mixed phase cloud) it is to be expected that ash might provide the best fit to the measurements by chance alone. With this proviso in mind, Figure 18 shows the retrieved optical depth, cloud top height, the effective radius and the retrieval cost, for those pixels picked as ash. Retrieval cost is a measure of the quality of the data. High quality retrievals have a cost of about one. For the Eyjafjallajökull eruption, a major issue is the ubiquity of thin layers of ash over thick liquid water cloud (often under a pronounced temperature inversion). These locations are identified by a high cost in the single layer retrieval.

The retrieved cloud top height for the ash plume in this scene ranges from approximately 6.5 km close to the volcano, down to approximately 2.5 km near the southern edge of the image. The areas of the ash plume associated

with the convective clouds apparent in the false colour image show a much higher altitude than the surrounding plume and often have been selected as ice cloud rather than ash. This seems a reasonable result, but is an example of where the assumptions of the retrieval have broken down. Examination of the retrieval cost shows that the regions where the false colour image shows that both ash and water cloud are present have greatly elevated cost, indicating the retrieval did not produce a good fit to the measurements, and is probably inaccurate - in this case the retrieved height is probably an intermediate level between an ash layer and the height of underlying water cloud. In these cases the retrieved optical depth and effective radius also show artefacts associated with the presence of cloud. Ignoring those retrievals whose cost is greater than two suggests that within the first ~ 500 km of the plume its height was in the range 2.5-6.5 km, the optical depth was 1-2.5 and the effective radius was 3-7 μm. The retrieved effective radius are typical of those reported for other eruptions given in Table 2.

An interesting feature of the plume, which is apparent in its East-West aligned portion is the strong gradient in effective radius and cloud top height along its southern edge, which is associated with a distinct change in the appearance of the plume in the false colour image. The retrieval of larger particles at a lower altitude along this edge suggests that there may have been a vertical wind shear acting on the plume, as larger particles would be expected to be found lower in the plume due to their higher settling velocity, resulting in subtly different trajectories for particles of different sizes. However, it is also possible that this feature is an artefact caused by the breakdown of the plane-parallel approximation near the edge of the plume, so no firm conclusion can be drawn from these results alone.

Figure 19 shows the ash mass density derived from the ORAC estimates of optical depth and effective radius using Equation (13). The grey values are obvious cloud contamination and have values in the range of about 50 - 80 $\mathrm{g\,m^2}$. The total mass in the scene is 0.83 Tg if the cloud contamination is included and 0.24 Tg, if all the pixels with an ash density of greater than 20 $\mathrm{g\,m^2}$ are ignored. Given the plume covers about 12 hours of emissions this represents an emission rate of 1.8×10^7 $\mathrm{g\,s^{-1}}$. This value is very similar to the 6th of May 2010 emission value of 2.0×10^7 $\mathrm{g\,s^{-1}}$ reported by Stohl et al. (2011).

Extended ORAC-SEVIRI Retrieval of the 2010 Eyjaf-jallajökull Ash Plume Overlying Clouds

By modifying the look-up-tables the ORAC cloud scheme is also applicable to measurements by MSG SEVIRI. As with the AATSR work, ORAC was first applied in the standard manner, fitting the optical depth, effective radius and altitude of a single-layer cloud model, considered to be infinitesimally geometrically thin in the vertical. The scheme was applied three times, assuming optical properties of (i) liquid cloud (ii) ice cloud and (iii) volcanic ash in turn. Measurements in all SEVIRI channels were used except the 3.92 and 9.66 μm channels. The cloud type present in each scene was identified by selecting the retrieval with the most consistent match to observations in all channels (as measured by the optimal estimation cost function), again in a similar fashion to the AATSR retrievals.

While this approach was successful in simple scenes, as was noted in the AATSR analysis, the ash plume often occurred over low lying (optically thick) liquid cloud and in these circumstances the retrieved height was significantly lower than that observed by the (Cloud-Aerosol Lidar with Orthogonal Polarization) CALIOP lidar. This is an issue which also affects the standard cloud retrieval, when thin ice cloud is present over thicker liquid cloud: In these circumstances the scheme will fit an effective height which lies between the uppermost cloud top and the lowest cloud base, generally at an altitude which corresponds to approximately one optical depth from the top (Siddans et al.; 2010; Poulsen et al.; 2011). Usually multi-layer cloud (both ice over liquid and ash over liquid) can be recognised, and flagged as unreliable, by examining the retrieval cost, since in most cases the multi-layer scene cannot be well represented by any of the single-layer models fitted.

An alternative approach is to run a two-layer scheme when the retrieval cost exceeds some pre-determined level. The two layer scheme includes an extended version of the ORAC forward model (Siddans et al.; 2010) which represents a second cloud layer, also in terms of its optical depth, effective radius and height. The retrieval state vector is extended to include these three additional parameters, however it is not generally feasible to obtain reliable information on all three quantities for both cloud layers. Here the problem is constrained by assuming the lower layer of liquid cloud to be optically thick and have effective radius of 10 μm. Only the height, of the lower layer cloud is retrieved, together with the height, radius and optical depth of the upper layer. Sensitivity to the actual optical depth and effective radius of the lower layer is avoided by only using thermal infrared channels in the two-layer scheme (as demonstrated for water cloud in Watts et al.; 2011). This retrieval relies on the fact that SEVIRI has thermal infrared channels

which are selectively sensitive to cloud at different altitudes because of the varying levels of trace-gas absorption in each channel. In particular, water vapour absorption in the 6.3 and 7.3 μm channels and CO_2 absorption at 13 μm gives information on height complementary to that from the window channels at 8.7, 11 and 12 μm. Furthermore, the spectral dependencies of cloud/ash optical properties provide distinct information on cloud optical depth and, to a lesser extent, particle size.

This scheme is applied twice: once assuming the upper layer to be ice and once assuming it to be ash. The result of these two retrievals which gives the best fit (lowest cost) to the observations is selected as being the most appropriate model for the upper layer.

This approach was trialled on SEVIRI image of the Eyjafjallajökull plume observed at 14:00 on 7 May 2010. Figure shows the SEVIRI retrieved height compared to CALIOP lidar backscatter profile (at 0.532 μm). CALIOP shows an ash plume from about 6 to 9 km in altitude, mainly between 47 and 49 N, though possibly extending further north at a slightly lower altitude, with amounts close to the noise level. CALIOP also shows an optically thick layer of liquid cloud at an altitude of 1 km across the whole section. The single layer scheme identifies the main part of this ash plume consistently but estimates low altitude and high optical depth. The two-layer scheme has been run for scenes in which the retrieval cost function is more than two times the expected value based on the modelled instrument noise and estimated forward model accuracy. For these scenes, the two-layer scheme returns a more correct estimate of the ash plume height ash and also detects the presence of ash between 49.5 and 50N (though here the height remains apparently underestimated). While it is not possible to directly validate the retrieved optical depths it is clear that the single layer scheme retrieves a value approximating the total optical depth of the ash (or ice) and underlying liquid cloud, while the two layer result gives a more plausible estimate for the thin ash layer.

Conclusions

In this paper new algorithms have been presented which provide volcanic plume properties from measurements by the MIPAS, AATSR and SEVIRI. A singular vector decomposition method, developed for the MIPAS, has been applied to observations of ash clouds from the eruptions of Nabro and Puyehue-Cordón Caulle in mid 2011. The geographical locations of the clouds based on MIPAS were in agreement with observations obtained by other methods. The SVD method provides a far more powerful tool for flagging

volcanic ash from space than was previously available. Weaker signals, and signals which have been partially masked by other effects are more easily observed. Periodic recalculation of the volcanic singular vectors through the course of an event suggested a change in aerosol composition as the plume aged for the Puyehue-Cordón Caulle but not for the Nabro plume. This was consistent with the first eruption being sulphur rich leading to a change in cloud composition from ash to sulphate.

The identification of ash plume height is a critical for the initialisation of algorithms that numerically model the evolution and transport of a volcanic plume. The MIPAS results suggest an altitude of about 15 km for the initial 2011 Puyehue-Cordón Caulle plume which was higher than the 12.7 km height estimated from the plume shadow. The latter value is in better agreement with a new algorithm SAPHRA that gives a main plume height 11.9 ± 1.4 km using the parallax between images provided by AATSR.

The SAPHRA approach lends itself to near-real-time application, as it is inherently simple and doesn't rely on any information beyond the ATSR radiances themselves. It could be envisaged that the algorithm could form the basis for an operational product which would detect and report the height of volcanic ash plumes detected by AATSR (and later SLSTR) on a routine basis. Despite the lack of daily global coverage, this information could very valuable in helping to constrain the dispersion models used by the VAAC centres to issue volcanic hazard warnings.

The quantitative use of satellite imagery and the full exploitation of high resolution spectral measurements of ash depends upon knowing the optical properties of the observed ash. Laboratory measurements of ash from the 1993 eruption of Mt Aso, Japan have been used to determine the refractive indices from 1 to 20 μm. The refractive indices have been used to retrieve ash properties from the AATSR and SEVIRI instruments using two versions of the ORAC algorithm.

For AATSR, a new cloud type in ORAC was used in the analysis of the plume from the 2011 Eyjafjallajökull eruption giving retrieved values of plume height 2.5 - 6.5 km, optical depth 1 - 2.5 and effective radius 3 -7 μm which were in agreement with other observations. A weakness of the algorithm occurred when underlying cloud invalidated the assumption of a single cloud layer. In these cases the retrieval errors are underestimated because the approach neglects the inherent uncertainty caused by assuming the scene to be contain only a single cloud layer. This was rectified in a modified version of ORAC applied to SEVIRI. In this case an extra model of a cloud underlying the ash plume was included in the range of applied models. Because the two layer scheme explicitly takes into account the multi-layer nature of the scene, it reports much larger errors, but these are more

consistent with the observed discrepancies with CALIOP. In cases where the plume overlay cloud this new model worked well, showing good agreement with correlative CALIOP observations.

It should be noted that the ORAC retrieval, as it currently stands, has several weaknesses which limit its applicability to volcanic ash detection and characterisation, many of which it shares with other algorithms:

- ORAC assumes plane-parallel cloud in its forward model. Volcanic ash plumes are often not plane-parallel (as they are typically a narrow plume). This can result in significant biases in the retrieved parameters, including height.

- As with all ash detection schemes, in cases where ash is mixing with large quantities of either ice or liquid water, there will come a point where the ash cloud becomes indistinguishable from a normal water or ice cloud. Furthermore, even if the cloud is determined to be ash, the presence of water will alter its radiative properties and produce a bias in the retrieval.

- For optically thin ash, an accurate knowledge of the surface properties (particularly its reflectance) becomes important and the Lambertian surface reflectance assumption can become problematic. This can be improved through the use a forward model which includes a model of surface bidirectional reflectance distribution function. Such a model is being introduced for ORAC cloud retrievals, but the accuracy of the retrieval is still dependant on prior knowledge of the surface reflectance.

- The retrieval of multi-layer cloud systems is still experimental and there remain obstacles to its wide spread application, not least the reliable detection of multi-layer scenes.

- The need for knowledge of the atmospheric temperature profile and composition, surface reflectance and suitable ash optical properties, as well as the computational cost of the scheme mean that ORAC is better suited to studying volcanic eruption plumes after the fact, rather than as a near real-time ash detection mechanism.

Despite these provisos, ORAC applied to ATSR offers a powerful tool for the characterisation of volcanic ash plumes, providing both an independent plume height estimate from the geometric method and estimates of the optical depth and effective radius of the ash, which can in turn be used to estimate ash mass loading.

References

Blong, R. (1984). *Volcanic hazards: a sourcebook on the effects of eruptions*, Academic Press, Sydney Orlando, Fla.

Burgess, A., Grainger, R. G. and Dudhia, A. (2006). Zonal mean atmospheric distribution of sulphur hexafluoride (SF_6), *Geophysical Research Letters* **33**.

Burton, M., Allard, P., Mure, F. and Oppenheimer, C. (2003). FTIR remote sensing of fractional magma degassing at Mount Etna, Sicily, *in* C. Oppenheimer, D. M. Pyle and J. Barclay (eds), *Volcanic Degassing*, Vol. 213 of *Geological Society Special Publication*, pp. 281–293.

Burton, M., Oppenheimer, C., Horrocks, L. and Francis, P. (2001). Diurnal changes in volcanic plume chemistry observed by lunar and solar occultation spectroscopy, *Geophysical Research Letters* **28**(5): 843–846.

CAA (2010). Volcanic ash, a briefing from the Civil Aviation Authority, `https://www.caa.co.uk/docs/2011/VolcanicAshBriefing.pdf`. accessed Dec 2011.

Casadevall, T. J. (ed.) (1994). *Volcanic Ash and Aviation Safety, Proc. 1st Int. Symp. on Volcanic Ash and Aviation Safety*, USGS Bulletin 2047, Washington.

Clarisse, L., Hurtmans, D., Prata, A. J., Karagulian, F., Clerbaux, C., De Maziere, M. and Coheur, P.-F. (2010). Retrieving radius, concentration, optical depth, and mass of different types of aerosols from high-resolution infrared nadir spectra, *Applied Optics* **49**(19): 3713–3722.

Corradini, S., Spinetti, C., Carboni, E., Tirelli, C., Buongiorno, M. F., Pugnaghi, S. and Gangale, G. (2008). Mt. Etna tropospheric ash retrieval and sensitivity analysis using moderate resolution imaging spectroradiometer measurements, *Journal of Applied Remote Sensing* **2**.

Durant, A. J., Bonadonna, C. and Horwell, C. J. (2010). Atmospheric and environmental impact of volcanic particulates, *Elements* **6**(4): 235–240.

Edmonds, M., Herd, R., Galle, B. and Oppenheimer, C. (2003). Automated, high time-resolution measurements of so_2 flux at Soufriere Hills Volcano, Montserrat, *Bulletin of Volcanology* **65**(8): 578–586.

Egan, W., Hilgeman, T. and Pang, K. (1975). Ultraviolet complex refractive-index of Martian dust - Laboratory measurements of terrestrial analogs, *Icarus* **25**(2): 344–355.

Ellrod, G., Connell, B. and Hillger, D. (2003). Improved detection of airborne volcanic ash using multispectral infrared satellite data, *Journal of Geophysical Research - Atmospheres* **108**(D12).

EUMETSAT (2011). EUMETSAT - image gallery, `http://oiswww.eumetsat.org/IPPS/html/MSG/RGB/ASH/ETHIOPIA/index.htm`. accessed June 2011.

European Commission (2010). *The Impact of the Volcanic Ash Cloud Crisis on the Air Transport Industry*, SEC(2010) 533, 27 April, Brussels.

Filizzola, C., Lacava, T., Marchese, F., Pergola, N., Scaffidi, I. and Tramutoli, V. (2007). Assessing RAT (Robust AVHRR Techniques) performances for volcanic ash cloud detection and monitoring in near real-time: The 2002 eruption of Mt. Etna (Italy), *Remote Sensing of the Environment* **107**(3): 440–454.

France-Presse, A. (2011). `http://ph.news.yahoo.com/volcanic-ash-cloud-grounds-more-flights-argentina-161459262.html`. accessed Dec. 2011.

Francis, P. and Rothery, D. (2000). Remote sensing of active volcanoes, *Annual Review of Earth and Planetary Sciences* **28**: 81–106.

Gabrielli, P., Barbante, C., Plane, J. M. C., Boutron, C. F., Jaffrezo, J. L., Mather, T. A., Stenni, B., Gaspari, V., Cozzi, G., Ferrari, C. and Cescon, P. (2008). Siderophile metal fallout to Greenland from the 1991 winter eruption of Hekla (Iceland) and during the global atmospheric perturbation of Pinatubo, *Chemical Geology* **255**(1-2): 78–86.

Gangale, G., Prata, A. J. and Clarisse, L. (2010). The infrared spectral signature of volcanic ash determined from high-spectral resolution satellite measurements, *Remote Sensing of the Environment* **114**(2): 414–425.

Global Volcanism Program (2011a). `http://www.volcano.si.edu/world/volcano.cfm?vnum=1507-15=\&volpage=weekly`. accessed Dec. 2011.

Global Volcanism Program (2011b). `http://www.volcano.si.edu/world/volcano.cfm?vnum=0201-101\&volpage=weekly`. accessed Dec. 2011.

Global Volcanism Program (2011c). `http://www.volcano.si.edu/world/volcano.cfm?vnum=1702-02=\&volpage=weekly`. accessed Dec. 2011.

Hale, G. M. and Querry, M. R. (1973). Optical constants of water in the 200-nm to 200-μm wavelength region, *Applied Optics* **12**: 555–563.

Heiken, G. and Wohletz, K. H. (1985). *Volcanic ash*, University of California Press, Berkeley.

Hirn, B., Di Bartola, C. and Ferrucci, F. (2009). Combined use of SEVIRI and MODIS for detecting, measuring, and monitoring active lava flows at erupting volcanoes, *IEEE Transactions on Geoscience and Remote Sensing* **47**(8): 2923–2930.

Horwell, C. J. and Baxter, P. J. (2006). The respiratory health hazards of volcanic ash: a review for volcanic risk mitigation, *Bulletin of Volcanology* **69**(1): 1–24.

Hurley, J., Dudhia, A. and Grainger, R. G. (2009). Cloud detection for MIPAS using singular vector decomposition, *Atmospheric Measurement Techniques* **2**(2): 533–547.

Hurley, J., Dudhia, A. and Grainger, R. G. (2011). Retrieval of macrophysical cloud parameters from MIPAS: algorithm description, *Atmospheric Measurement Techniques* **4**(4): 683–704.

Ilyinskaya, E., Oppenheimer, C., Mather, T. A., Martin, R. S. and Kyle, P. R. (2010). Size-resolved chemical composition of aerosol emitted by Erebus volcano, Antarctica, *Geochemistry Geophysics Geosystems* **11**.

Jones, M. T. and Gislason, S. R. (2008). Rapid releases of metal salts and nutrients following the deposition of volcanic ash into aqueous environments, *Geochemica et Cosmochimica Acta* **72**(15): 3661–3680.

Krotkov, N. A., Flittner, D. E., Krueger, A. J., Kostinski, A., Riley, C., Rose, W. and Torres, O. (1999). Effect of particle non-sphericity on satellite monitoring of drifting volcanic ash clouds, *Journal of Quantitative Spectroscopy and Radiative Transfer* **63**(2-6): 613–630.

Lean, K. (2009). Empirical methods for detecting atmospheric aerosol events from satellite measurements, *Technical report*, Department of Physics, University of Oxford.

Luo, B., Krieger, U. K. and Peter, T. (1996). Densities and refractive indices of $H_2SO_4/HNO_3/H_2O$ solutions to stratospheric temperatures, *Geophysical Research Letters* **23**(25): 3707–3710.

Martin, R. S., Mather, T. A., Pyle, D. M., Power, M., Allen, A. G., Aiuppa, A., Horwell, C. J. and Ward, E. P. W. (2008). Composition-resolved size distributions of volcanic aerosols in the Mt. Etna plumes, *Journal of Geophysical Research* **113**(D17): D17211.

Martin, R. S., Watt, S. F. L., Pyle, D. M., Mather, T. A., Matthews, N. E., Georg, R. B., Day, J. A., Fairhead, T., Witt, M. L. I. and Quayle, B. M. (2009). Environmental effects of ashfall in Argentina from the 2008 Chaiten volcanic eruption, *Journal of Volcanology and Geothermal Research* **184**(3-4): 462–472.

Marzano, F. S., Lamantea, M., Montopoli, M., Fabio, S. D. and Picciotti, E. (2011). The Eyjafjöll explosive volcanic eruption from a microwave weather radar perspective, *Atmospheric Chemistry and Physics* **11**(18): 9503–9518.

Mather, T. A., Pyle, D. M. and Oppenheimer, C. (2003). Tropospheric Volcanic Aerosol, *in* A. Robock and C. Oppenheimer (eds), *Volcanism and the Earth's Atmosphere*, AGU Geophysical Monograph 139, American Geophysical Union, Washington, D.C., pp. 189–212.

Mazzocchi, M., Hansstein, F. and Ragona, M. (2010). The 2010 volcanic ash cloud and its financial impact on the European airline industry, *CESifo Forum* **11**: 92–100.

Moroney, C., Davies, R. and Muller, J. P. (2002). Operational retrieval of cloud-top heights using misr data, *IEEE Transactions on Geoscience and Remote Sensing* **40**: 1532–1540.

Muller, J., Mandanayake, A., Moroney, C., Davies, R., Diner, D. and Paradise, S. (2002). MISR stereoscopic image matchers: Techniques and results, *IEEE Transactions on Geoscience and Remote Sensing* **40**(7): 1547–1559.

Muller, J. P., Denis, M. A., Dundas, R. D., Mitchell, K. L., Naud, C. and Mannstein, H. (2007). Stereo cloud-top heights and cloud fraction retrieval from ATSR-2, *International Journal of Remote Sensing* **28**(9): 1921–1938.

NASA Earth Observatory (2011). `http://earthobservatory.nasa.gov/IOTD/view.php?id=50996`. accessed Dec. 2011.

National Oceanic and Atmospheric Administration, National Aeronautics and Space Adminsitration and United States Airforce (1976). *U.S. Standard Atmosphere*, U.S. Government Printing Office, Washington, D.C.

Observatorio Volcanologico de los Andes del Sur (OVDAS)(Chile) (2011). `http://www2.sernageomin.cl/ovdas/ovdas7/ovdas66.php`. accessed Dec. 2011.

Ono, K., Watanabe, K., Hoshizumi, H. and ichiro Ikebe, S. (1995). Ash eruption of the Naka-dake crater, Aso volcano, southwestern Japan, *Journal of Volcanology and Geothermal Research* **66**: 137–148.

Oppenheimer, C. (1998). Volcanological applications of meteorological satellites, *International Journal of Remote Sensing* **19**(15): 2829–2864.

Oppenheimer, C., Bani, P., Calkins, J. A., Burton, M. R. and Sawyer, G. M. (2006). Rapid FTIR sensing of volcanic gases released by Strombolian explosions at Yasur volcano, Vanuatu, *Applied Physics B - Lasers and Optics* **85**(2-3): 453–460.

Oppenheimer, C., Kyle, P., Eisele, F., Crawford, J., Huey, G., Tanner, D., Kim, S., Mauldin, L., Blake, D., Beyersdorf, A., Buhr, M. and Davis, D. (2010). Atmospheric chemistry of an Antarctic volcanic plume, *Journal of Geophysical Research - Atmospheres* **115**.

Patterson, E. M. (1981). Measurements of the imaginary part of the refractive index between 300 and 700 nanometers for Mount St. Helens ash, *Science* **211**(4484): 836–838.

Patterson, E. M. (1994). Optical absorption coefficients of soil-aerosol particles and volcanic ash between 1 and 16 μm, *Proceedings of the Second Conference on Atmospheric Radiation*, American Meteorological Society, pp. 177–180.

Patterson, E. M., Pollard, C. O. and Galindo, I. (1983). Optical-properties of the ashes from El-Chichon volcano, *Geophysical Research Letters* **10**(4): 317–320.

Payne, V. H., Noone, D., Dudhia, A., Piccolo, C. and Grainger, R. G. (2007). Global satellite measurements of HDO and implications for understanding the transport of water vapour into the stratosphere, *Quarterly Journal of the Royal Meteorological Society* **133**: 1459–1471.

35

Pollack, J. B., Toon, O. B. and Khare, B. N. (1973). Optical properties of some terrestrial rocks and glasses, *Icarus* **19**(3): 372–389.

Poulsen, C. A., Watts, P., Thomas, G. E., Sayer, A. M., Siddans, R., Grainger, R. G., Lawrence, B. N., Campmany, E., Dean, S. M. and Arnold, C. (2011). Cloud retrievals from satellite data using optimal estimation: evaluation and application to ATSR, *Atmospheric Measurement Techniques Discussions* **4**: 2389–2431.

Prata, A. J. (1989a). Infrared radiative transfer calculations for volcanic ash clouds, *Geophysical Research Letters* **16**: 1293–1296.

Prata, A. J. (1989b). Observations of volcanic ash clouds in the 10-12 μm window using AVHRR/2 data, *International Journal of Remote Sensing* **10**: 751–761.

Prata, A. J., Bluth, G. J. S., Rose, W. I., Schneider, D. J. and Tupper, A. C. . (2001). Comments on "Failures in detecting volcanic ash from a satellite-based technique", *Remote Sensing of the Environment* **78**: 341–346.

Prata, A. J. and Grant, I. F. (2001). Retrieval of microphysical and morphological properties of volcanic ash plumes from satellite data: Application to Mt Ruapehu, New Zealand, *Quarterly Journal of the Royal Meteorological Society* **127**: 2153–2179.

Prata, A. J. and Kerkmann, J. (2007). Simultaneous retrieval of volcanic ash and SO(2) using MSG-SEVIRI measurements, *Geophysical Research Letters* **34**(5).

Press, W. H., Teukolsky, S. A., Vetterling, W. T. and Flannery, B. P. (1992). *Numerical Recipes in C : The Art of Scientific Computing*, Cambridge University Press, Cambridge Cambridgeshire New York.

Read, W., Froidevaux, L. and Waters, J. (1993). Microwave limb sounder measurements of stratospheric SO$_2$ from the Mt Pinatubo volcano, *Journal of Geophysical Research* **20**: 1299–1302.

Riley, C. M., Rose, W. I. and Bluth, G. J. S. (2003). Quantitative shape measurements of distal volcanic ash, *Journal of Geophysical Research* **108**(B10): 2504.

Rose, W., Bluth, G. and Ernst, G. (2000). Integrating retrievals of volcanic cloud characteristics from satellite remote sensors: a summary, *Philosophical Transactions of the Royal Society of London Series A - Mathematical Physical and Engineering Sciences* **358**(1770): 1585–1606.

Rose, W. I. and Durant, A. J. (2009). Fine ash content of explosive eruptions, *Journal of Volcanology and Geothermal Research* **186**(1-2): 32–39.

Rose, W. I., Gu, Y., Watson, I. M., Yu, T., Bluth, G. J. S., Prata, A. J., Krueger, A. J., Krotkov, N., Carn, S., Fromm, M. D., Hunton, D. E., Ernst, G. G. J., Viggiano, A. A., Miller, T. M., Ballenthin, J. O., Reeves, J. M., Wilson, J. C., Anderson, B. E. and Flittner, D. E. (2003). The February-March 2000 eruption of Hekla, Iceland from a satellite perspective, *in* A. Robock and C. Oppenheimer (eds), *Volcanism and Earth's Atmosphere*, AGU Geophysical Monograph 139, American Geophysical Union, Washington, D.C., pp. 107–132.

Rust, A. C. and Cashman, K. V. (2011). Permeability controls on expansion and size distributions of pyroclasts, *Journal of Geophysical Research* **116**(B11): B11202.

Sawyer, G. M., Oppenheimer, C., Tsanev, V. I. and Yirgu, G. (2008). Magmatic degassing at Erta 'Ale volcano, Ethiopia, *Journal of Volcanology and Geothermal Research* **178**(4, SI): 837–846.

Sayer, A. M., Poulsen, C. A., Arnold, C., Campmany, E., Dean, S., Ewen, G. B. L., Grainger, R. G., Lawrence, B. N., Siddans, R., Thomas, G. E. and Watts, P. D. (2011). Global retrieval of ATSR cloud parameters and evaluation (GRAPE): dataset assessment, *Atmospheric Chemistry and Physics* **11**(8): 3913–3936.

Scandone, R., Cashman, K. V. and Malone, S. D. (2007). Magma supply, magma ascent and the style of volcanic eruptions, *Earth and Planetary Science Letters* **253**(3-4): 513–529.

Schmid, R. (1981). Descriptive nomenclature and classification of pyroclastic deposits and fragments: Recommendations of the iugs subcommission on the systematics of igneous rocks, *Geology* **9**(1): 41–43.

Seftor, C. J., Hsu, N. C., Herman, J. R., Bhartia, P. K., Torres, O., Rose, W. I., Schneider, D. J. and Krotkov, N. (1997). Detection of volcanic ash clouds from Nimbus 7 /total ozone mapping spectrometer, *Journal of Geophysical Research* **102**: 16749–16759.

Servicio Nacional de Geologia y Mineria (2011a). `http://www2.sernageomin.cl/ovdas/ovdas7/informativos2/Informes/Reportes/RegionXIV/REAV\_N13\_Los-Rios\_27042011.pdf`. accessed Dec. 2011.

Servicio Nacional de Geologia y Mineria (2011b). `http://www2.sernageomin.cl/ovdas/ovdas7/informativos2/Informes/Reportes/RegionXIV/REAV\_N26\_Los-Rios\_03062011.pdf`. accessed Dec. 2011.

Servicio Nacional de Geologia y Mineria (2011c). `http://www2.sernageomin.cl/ovdas/ovdas7/informativos2/Informes/Reportes/RegionXIV/REAV\_N27\_Los-Rios\_04062011.pdf`. accessed Dec. 2011.

Servicio Nacional de Geologia y Mineria (2011d). `http://www2.sernageomin.cl/ovdas/ovdas7/informativos2/Informes/Reportes/RegionXIV/REAV\_N28\_Los-Rios\_04062011.pdf`. accessed Dec. 2011.

Sheridan, M. F. and Wohletz, K. H. (1983). Hydrovolcanism - basic considerations and review, *Journal of Volcanology and Geothermal Research* **17**(1-4): 1–29.

Sicard, M., Guerrero-Rascado, J. L., Navas-Guzmán, F., Preißler, J., Molero, F., Tomás, S., Bravo-Aranda, J. A., Comerón, A., Rocadenbosch, F., Wagner, F., Pujadas, M. and Alados-Arboledas, L. (2011). Monitoring of the Eyjafjallajökull volcanic aerosol plume over the Iberian Peninsula by means of four EARLINET lidar stations, *Atmospheric Chemistry and Physics Discussions* **11**: 29681–29721.

Siddans, R., Poulsen, C. and Carboni, E. (2010). Cloud model for operational retrievals from MSG SEVIRI, *Technical report*, European Organisation for the Exploitation of Meteorololgical Satellites.

Sigmundsson, F., Hreinsdóttir, S., Hooper, A., Árnadóttir, T., Pedersen, R., Roberts, M. J., Óskarsson, N., Auriac, A., Decriem, J., Einarsson, P., Geirsson, H., Hensch, M., Ófeigsson, B. G., Sturkell, E., Sveinbjörnsson, H. and Feigl, K. L. (2010). Intrusion triggering of the 2010 Eyjafjallajökull explosive eruption, *Nature* **468**: 426–432.

Singer, B. S., Jicha, B. R., Harper, M. A., Naranjo, J. A., Lara, L. E. and Moreno-Roa, H. (2008). Eruptive history, geochronology, and magmatic evolution of the Puyehue-Cordón Caulle volcanic complex, Chile, *Geological Society of America Bulletin* **120**: 599–618.

Solomon, S., Qin, D., Manning, M., Chen, Z., Marquis, M., Averyt, K. B., Tignor, M. and Miller, H. L. (eds) (2007). *Climate Change 2007: The Physical Science Basis: contribution of Working Group I to the Fourth Assessment Report of the Intergovernmental Panel on Climate Change*, Cambridge University Press, Cambridge New York.

Spang, R., Remedios, J. J., Kramer, L. J., Poole, L. R., Fromm, M. D., Müller, M., Baumgarten, G. and Konopka, P. (2005). Polar stratospheric cloud observations by MIPAS on ENVISAT: detection method, validation and analysis of the northern hemisphere winter 2002/2003, *Atmospheric Chemistry and Physics* **5**(3): 679–692.

Sparks, R. S. J. (1986). The dimensions and dynamics of volcanic eruption columns, *Bulletin of Volcanology* **48**: 3–15.

Sparks, R. S. J., Moore, J. G. and Rice, C. J. (1986). The initial giant umbrella cloud of the May 18th 1980, explosive eruption of Mt St Helens, *Journal of Volcanology and Geothermal Research* **28**(3-4): 257–274.

Spinetti, C., Corradini, S. and Buongiorno, M. F. (2007). Volcanic ash retrieval at Mt. Etna using AVHRR and MODIS data, *in* Ehlers, M and Michel, U (ed.), *Remote Sensing for Environmental Monitoring, GIS Applications, and Geology VII*, Vol. 6749 of *Proceedings of the Society of Photo-Optical Instrumentation Engineers (SPIE)*.

Stohl, A., Prata, A. J., Eckhardt, S., Clarisse, L., Durant, A., Henne, S., Kristiansen, N. I., Minikin, A., Schumann, U., Seibert, P., Stebel, K., Thomas, H. E., Thorsteinsson, T., Tørseth, K. and Weinzierl, B. (2011). Determination of time- and height-resolved volcanic ash emissions and their use for quantitative ash dispersion modeling: the 2010 Eyjafjallajökull eruption, *Atmospheric Chemistry and Physics* **11**(9): 4333–4351.

Taddeucci, J., Pompilio, M. and Scarlato, P. (2004). Conduit processes during the July-August 2001 explosive activity of Mt. Etna (Italy): inferences from glass chemistry and crystal size distribution of ash particles, *Journal of Volcanology and Geothermal Research* **137**(1-3): 33–54.

The Jerusalem Post (2011). Ash cloud from Eritrean volcano reaches Israel, `http://www.jpost.com/Headlines/Article.aspx?id=224929`. accessed Dec. 2011.

Thomas, G. E., Bass, S. F., Grainger, R. G. and Lambert, A. (2005). Retrieval of aerosol refractive index from extinction spectra with a damped harmonic-oscillator band model, *Applied Optics* **44**(7): 1332–1341.

Thomas, H. E. and Prata, A. J. (2011). Sulphur dioxide as a volcanic ash proxy during the April?May 2010 eruption of Eyjafjallajökull Volcano, Iceland, *Atmospheric Chemistry and Physics* **11**(14): 6871–6880.

Thomas, H. E. and Watson, I. M. (2010). Observations of volcanic emissions from space: current and future perspectives, *Natural Hazards* **54**(2): 323–354.

Toon, O. B., Pollack, J. B. and Sagan, C. (1977). Physical properties of the particles composing the Martian dust storm of 1971-1972, *Icarus* **30**(4): 663–696.

USGS Earthquake Hazards Program (2011). `http://earthquake.usgs.gov/`. accessed Dec. 2011.

Volz, F. E. (1973). Infrared optical constants of ammonium sulfate, Sahara dust, volcanic pumice and flyash, *Applied Optics* **12**: 564–568.

Walker, J. C., Carboni, E., Dudhia, A. and Grainger, R. G. (2012). Improved detection of sulphur dioxide in volcanic plumes using satellite-based hyperspectral infrared measurements: Application to the Eyjafjallajökull 2010 eruption, *Journal of Geophysical Research - Atmospheres* .

Warren, S. G. and Brandt, R. E. (2008). Optical constants of ice from the ultraviolet to the microwave: A revised compilation, *Journal of Geophysical Research* **113**(D14): D14220.

Watts, P. D., Bennartz, R. and Fell, F. (2011). Retrieval of two-layer cloud properties from multispectral observations using optimal estimation, *Journal of Geophysical Research* **116**(D16): D16203.

Wen, S. and Rose, W. I. (1994). Retrieval of sizes and total masses of particles in volcanic clouds using AVHRR bands 4 and 5, *Journal of Geophysical Research* **99**(D3): 5421–5431.

Wiart, P. and Oppenheimer, C. (2005). Large magnitude silicic volcanism in north Afar: the Nabro volcanic range and Ma'alalta volcano, *Bulletin of Volcanology* **67**: 99–115.

Witham, C. S., Hort, M. C., Potts, R., Servranckx, R., Husson, P. and Bonnardot, F. (2007). Comparison of VAAC atmospheric dispersion models using the 1 November 2004 Grimsvotn eruption, *Meteorological Applications* **14**(1): 27–38.

Wooster, M. J. and Rothery, D. A. (1997). Thermal monitoring of Lascar Volcano, Chile, using infrared data from the along-track scanning radiometer: A 1992-1995 time series, *Bulletin of Volcanology* **58**(7): 566–579.

Wooster, M., Rothery, D. A., Coltelli, M. and Buongiorno, M. F. (2000). High temperature thermal activity from MSG SEVIRI: volcanoes and fires, *in* R. A. Harris (ed.), *First MSG RAO Workshop, held 17-19 May, 2000, at CNR, Bologna, Italy*, European Space Agency ESASP-452.

Yu, T. X., Rose, W. I. and Prata, A. J. (2002). Atmospheric correction for satellite-based volcanic ash mapping and retrievals using "split window" IR data from GOES and AVHRR, *Journal of Geophysical Research* **107**(D16).

Yuan, T., Remer, L. A. and Yu, H. (2011). Microphysical, macrophysical and radiative signatures of volcanic aerosols in trade wind cumulus observed by the A-Train, *Atmospheric Chemistry and Physics* **11**(14): 7119–7132.

Zehner, C. (ed.) (2012). *Monitoring Volcanic Ash from Space. Proceedings of the ESA-EUMETSAT workshop on the 14 April to 23 May 2010 eruption at the Eyjafjoll volcano, South Iceland*, ESA STM-280, European Space Agency.

Table 1: Existing measurements of volcanic ash spectral complex refractive indices ($m = n - ik$).

Ash Sample	Refractive Index Component	Spectral Range (μm)	Reference
Mt. Spur	n and k	0.34, 0.36, 0.38	Krotkov et al. (1999)
Mt. St. Helens	k only	0.3-0.7	Patterson (1981)
Mayon	k only	1-16	Patterson (1994)
El Chichón	k only	0.3-0.7	Patterson et al. (1983)

Table 2: Eruption quantified using the brightness temperature difference.

Instrument	Eruption	r_e (μm)	Reference
ATSR-2	Mt Ruapehu, 1996	3 - 5.1[a]	Prata and Grant (2001)
AVHRR	Mt. Galunggung, July 1982		Prata (1989a,b)
AVHRR	El Chichón, 1982	4 - 8	Rose et al. (2000)
AVHRR	Cerro Hudson, 1991	6 - 9	Rose et al. (2000)
AVHRR	Mt Spurr, August 1992	2.4 - 3.15	Wen and Rose (1994)
AVHRR	Mt Spurr, August 1992	0.5 - 6	Yu et al. (2002)
AVHRR	Mt Spurr, August 1992		Krotkov et al. (1999)
AVHRR	Mt Etna, November 2006		Spinetti et al. (2007)
AVHRR	Mt Etna, October 2002		Filizzola et al. (2007)
GOES	Montserrat, December 1997	0.6 - 6	Yu et al. (2002)
MODIS	Mt Etna, November 2006	1.6 - 3.3	Spinetti et al. (2007); Corradini et al. (2008)

[a]Particle radii have been estimated from the reported mean radii by multiplying by 1.5; this is based on assuming a log-normal distribution with a spread of 1.5.
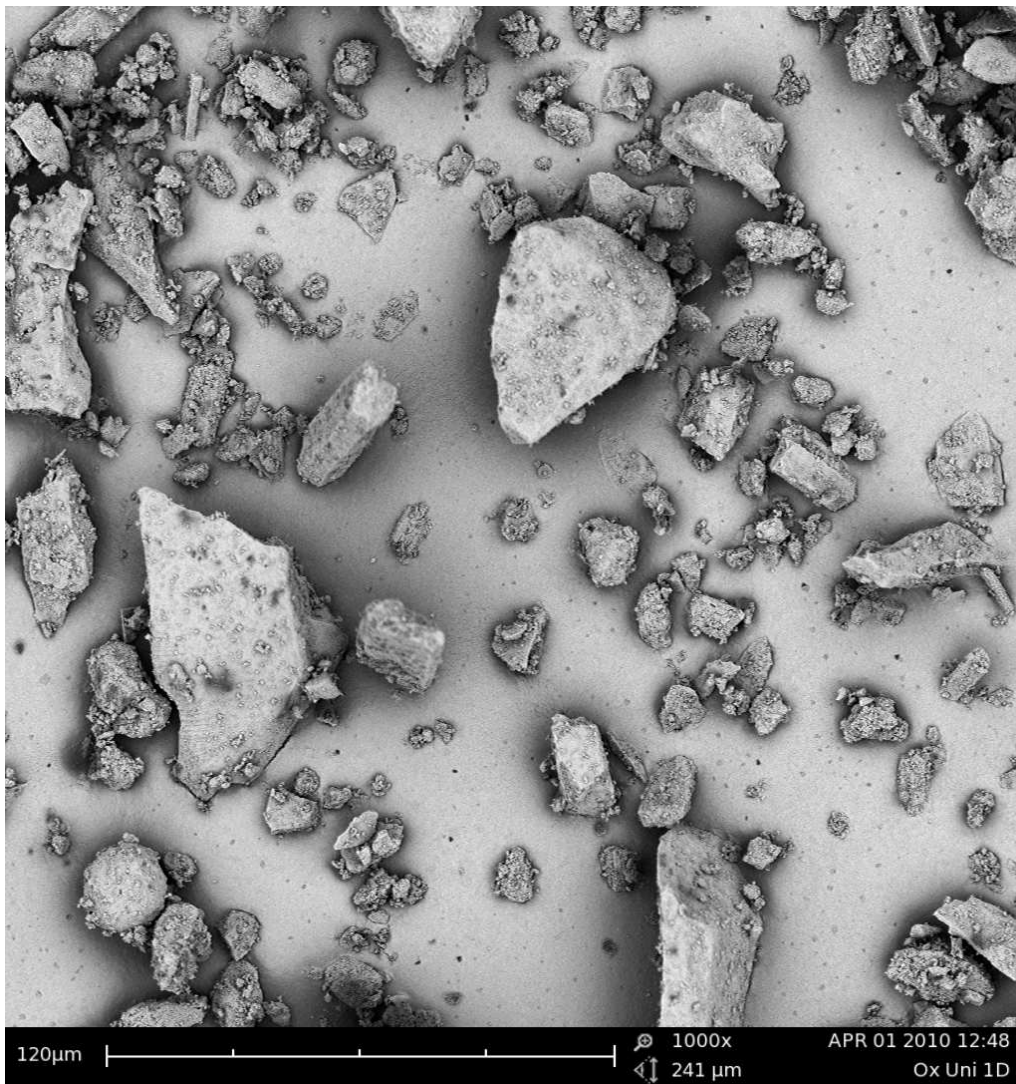
Figure 1: SEM micrograph of sieved (radius $< 22.5\,\mu$m) ash from the 1993 eruptions of Mt Aso, Japan. This sample was collected from a bomb-shelter where 1 - 2 m of ash had accumulated.
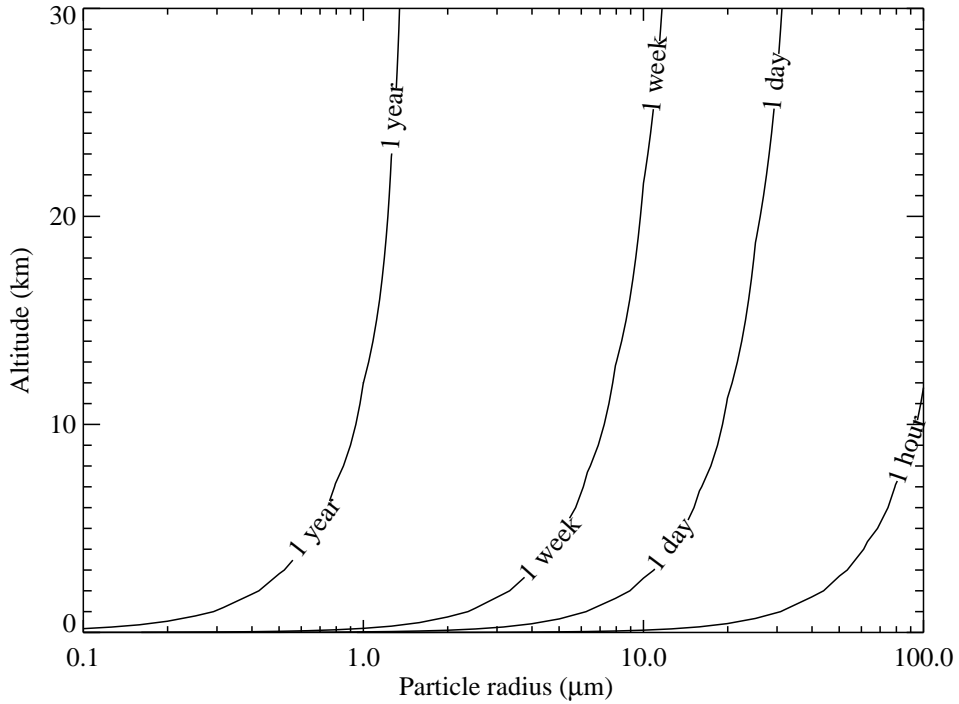
Figure 2: Fallout time calculated for spherical particles (density of 2.4 g cm^{-3}) as a function of particle radius and injection height based on the US Standard Atmosphere 1976 (National Oceanic and Atmospheric Administration, National Aeronautics and Space Adminsitration and United States Airforce; 1976).
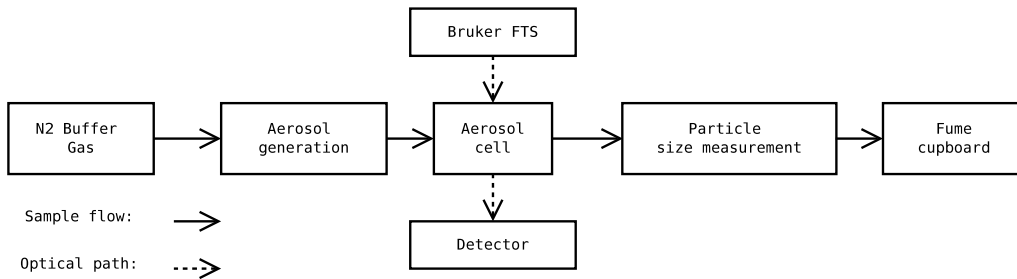
Figure 3: Simplified diagram of experimental configuration.
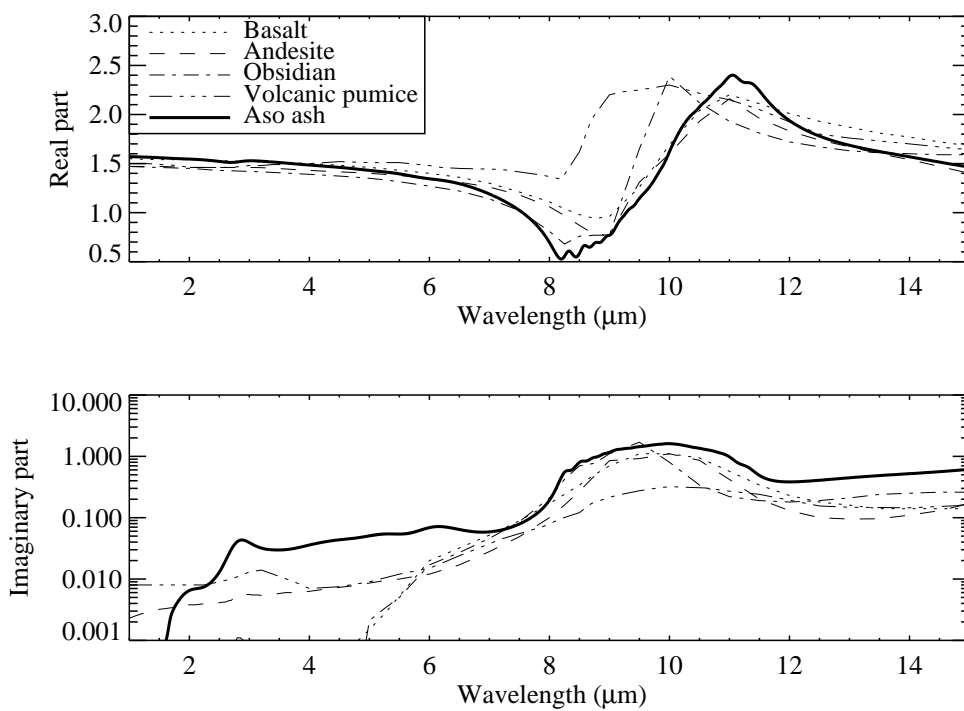
Figure 4: Real and imaginary refractive index components determined from an Aso ash sample. The refractive indices of basalt, andesite, obsidian (Pollack et al.; 1973) and volcanic pumice (Volz; 1973) are also shown.
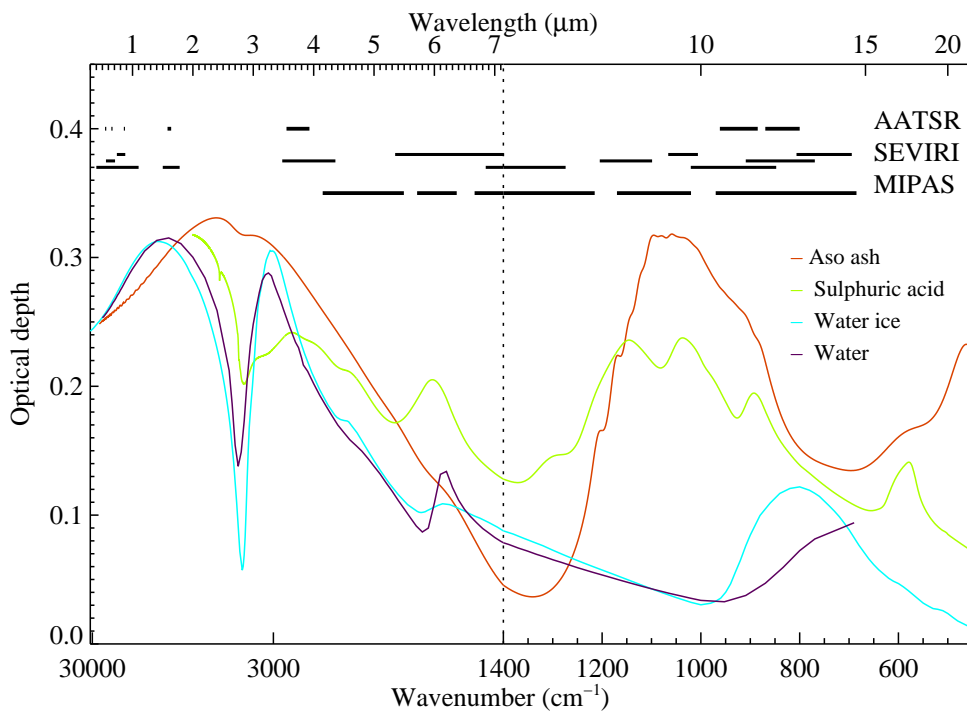
Figure 5: Simulated optical thickness for a 100 m thick plume consisting of a lognormal distribution ($N_0 = 2 \times 10^2$ cm^{-3}, $r_m = 1$ μm, $S = 1.7$) of spherical particles. The plume is assumed to consist of Aso ash (using the preliminary refractive indices), sulphuric acid (refractive indices from Luo et al.; 1996), water ice (refractive indices from Warren and Brandt; 2008) and water (refractive indices from Hale and Querry; 1973). The black lines at the top of the plot indicate the AATSR and SEVIRI channels and the MIPAS spectral range.
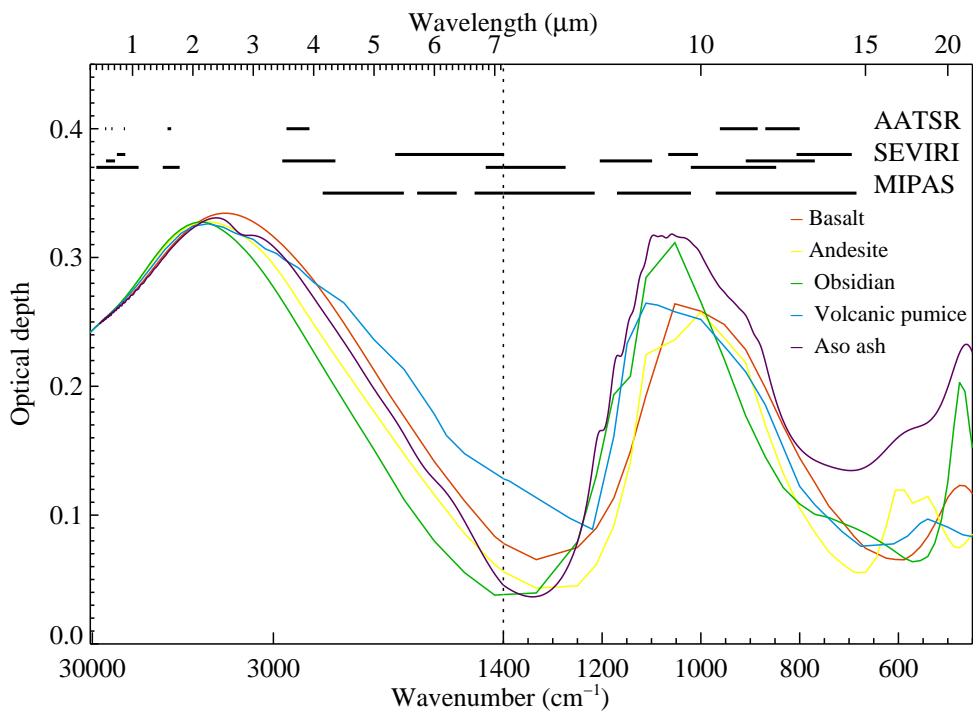
Figure 6: Optical depth as a function of wavenumber for a 100 m thick ash plume consisting of a lognormal distribution ($N_0 = 2,102$ cm^{-3}, $r_\mathrm{m} = 1$ μm, $S = 1.7$) of spherical particles of different composition. The chosen size distribution and plume thickness gives a column loading of 3.7 g m^{-2}. Refractive index data is from, Pollack et al. (1973) for basaltic glass, andesite and obsidian) and from Volz (1973) for pumice. The Aso values used the refractive indices given earlier. The black lines at the top of the plot indicate the AATSR and SEVIRI channels and the MIPAS spectral range.

47
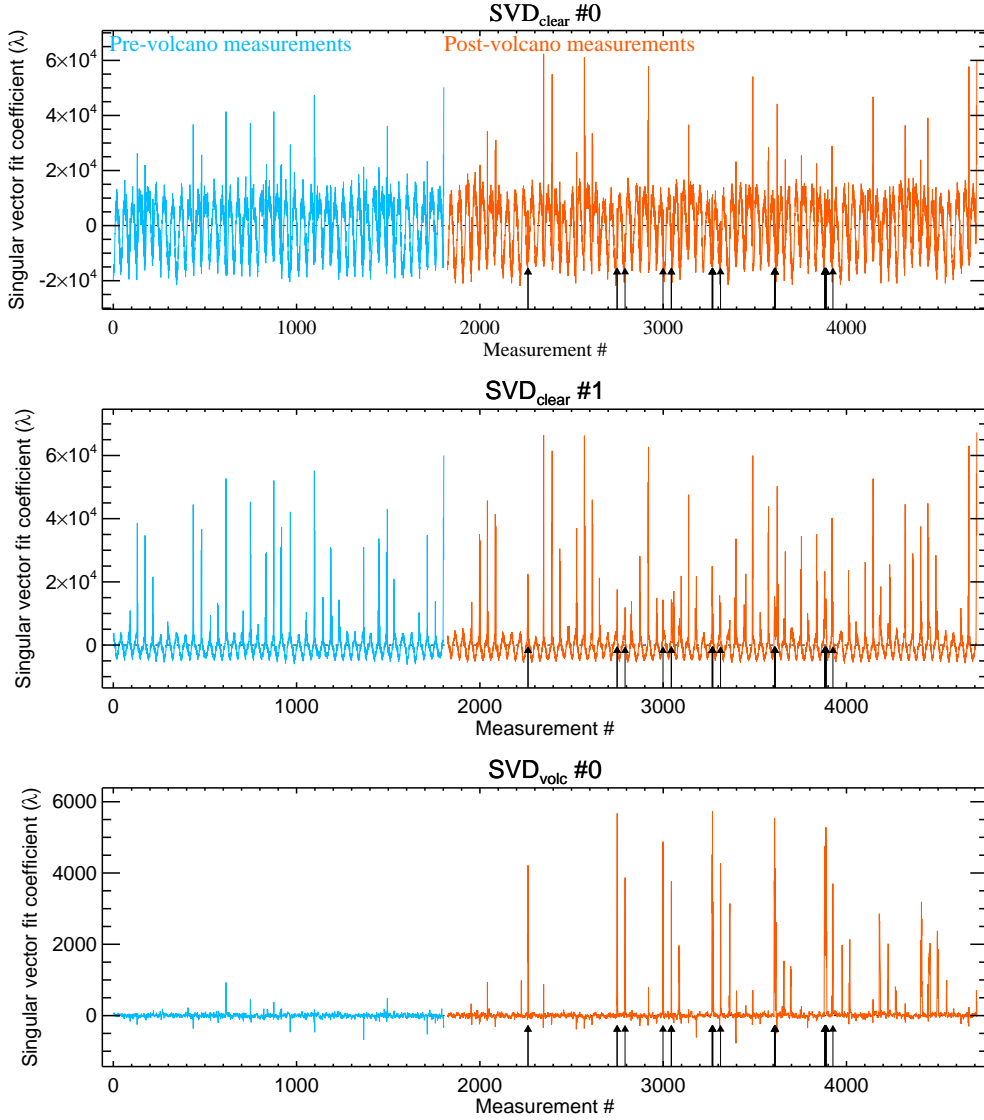
Figure 7: Fit coefficients, λ_i, for the first two clear singular vectors, and the first volcanic singular vector for the Nabro eruption at MIPAS tangent measurement heights of 15 ± 1.5 km. The x-axis gives an arbitrary measurement number (which is increasing in time). Data taken after the eruption are shown in orange. The diurnal cycle can be clearly seen in the top two vectors (which capture 70 % of variability). Arrows mark points where the volcanic plume was seen, using the test given in Equation 6. While the arrows mark the strongest signals, the SVD method is able to distinguish weaker volcanic signatures.
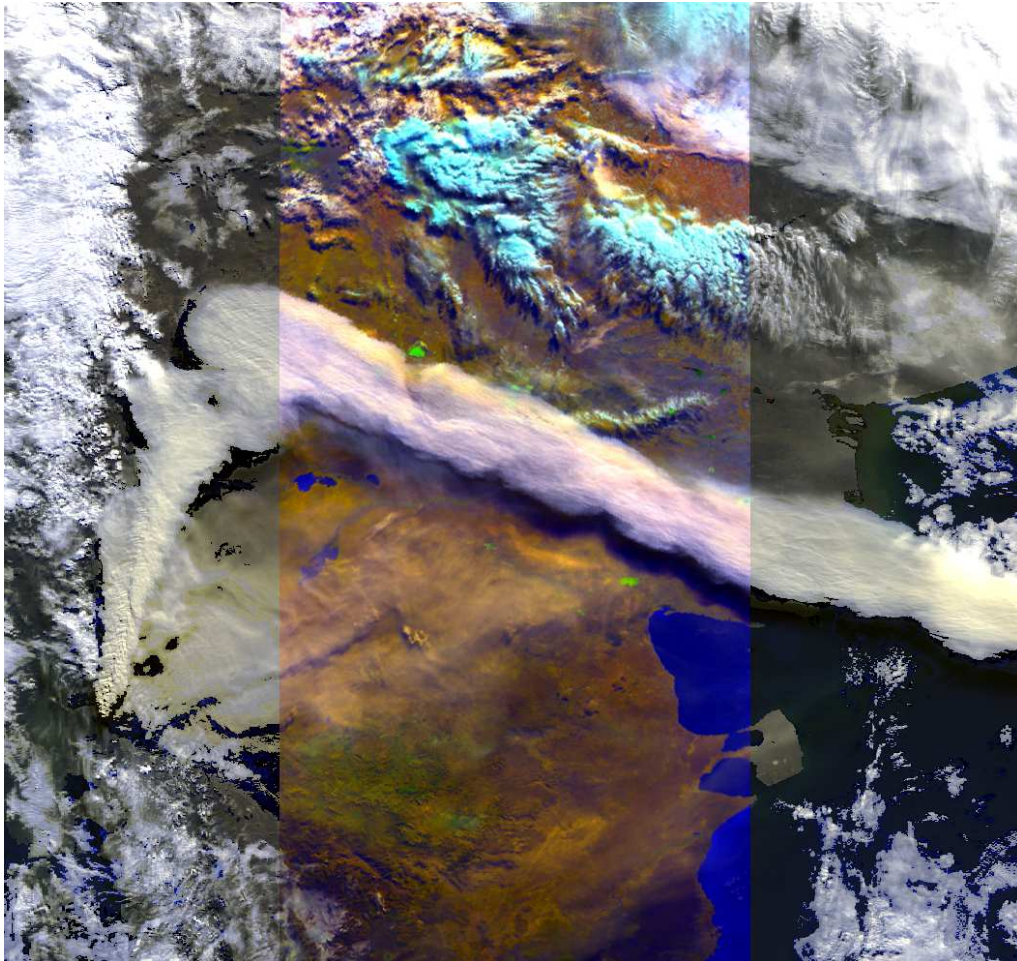
Figure 8: A combined AATSR-MERIS false colour image of the Puyehue-Cordn Caulle eruption plume taken at 14:01 GMT on the 6th June 2011. The central section of the image shows the AATSR nadir view, with the MERIS image providing context. The volcano itself is located in the left-hand section of the MERIS image, and the coast of Argentina is visible on the right. North is approximately towards the top of the image.

49
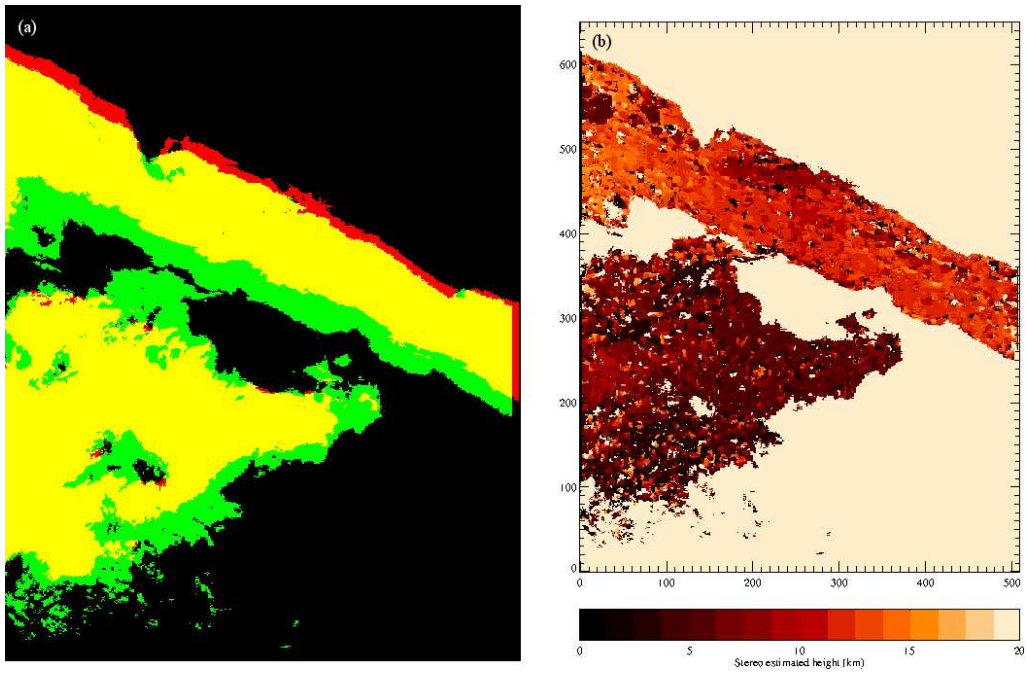
Figure 9: (a) The pixels determined to be ash from the AATSR image shown in Figure 16. Red denotes pixels detected in the nadir view only, green in the forward view only and yellow in both. The parallax between the two views is clear in the main northern plume, but, as one would expect, it is much less evident in the southern (much lower) plume. (b) The stereo-retrieved ash height from the ash plume shown in Figure 16.

50
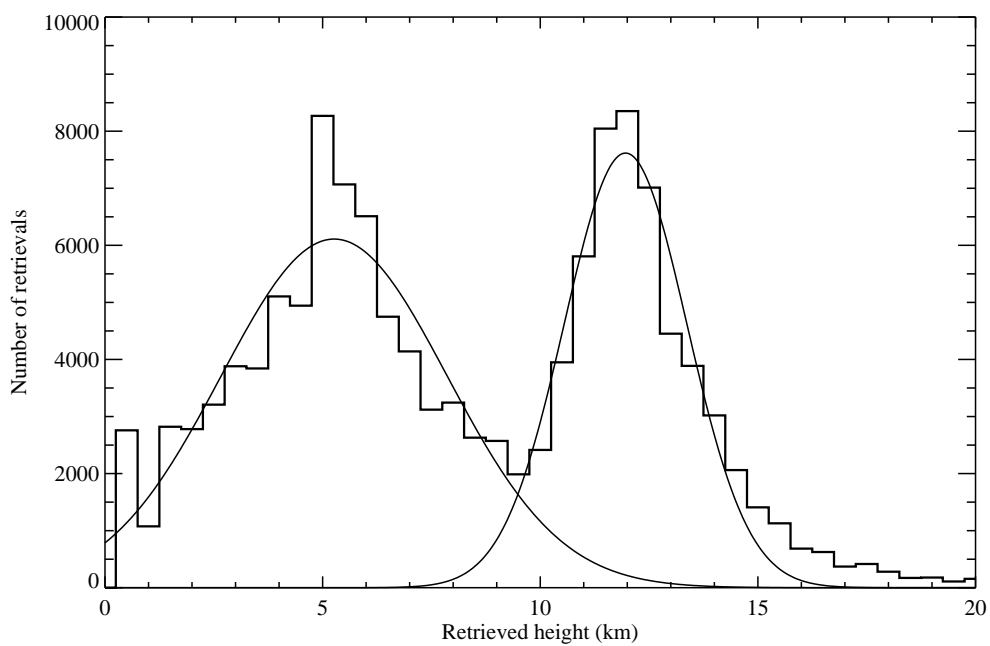
Figure 10: Histogram of the retrieved plume height shown in Figure 9b. Gaussians representing the mean height and uncertainty of both plumes are plotted.
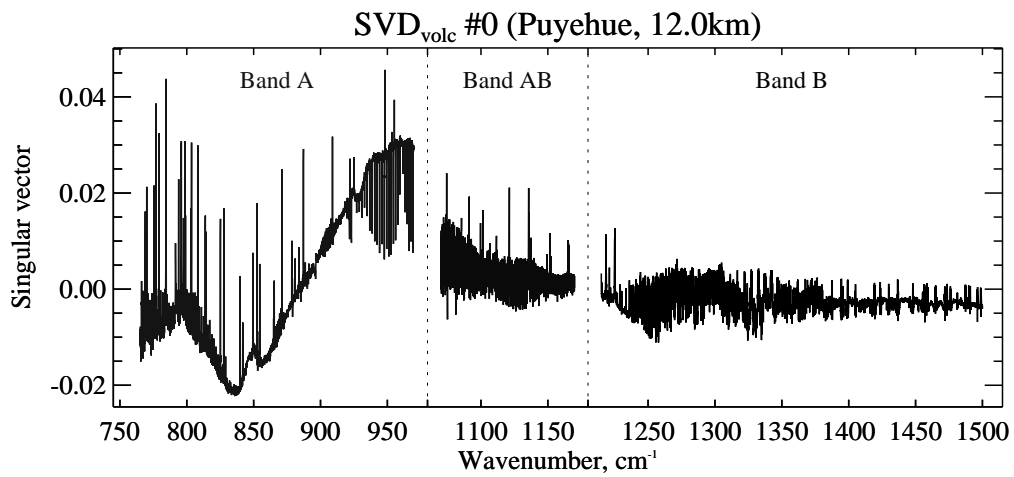
Figure 11: The principle volcanic singular vector for the Puyehue eruption, calculated using data from the week after the eruptions, when the empirical flag defined in Equation 6 is positive. The three shortest MIPAS wavenumber bands, A, AB, and B were fitted, but excluding the ozone region of AB band (1020-1070 cm^{-1}), and the beginning of the A band (685-765 cm^{-1}) where carbon dioxide and ozone absorption is extremely strong. Calculations were restricted to the latitude range 20-60° S.
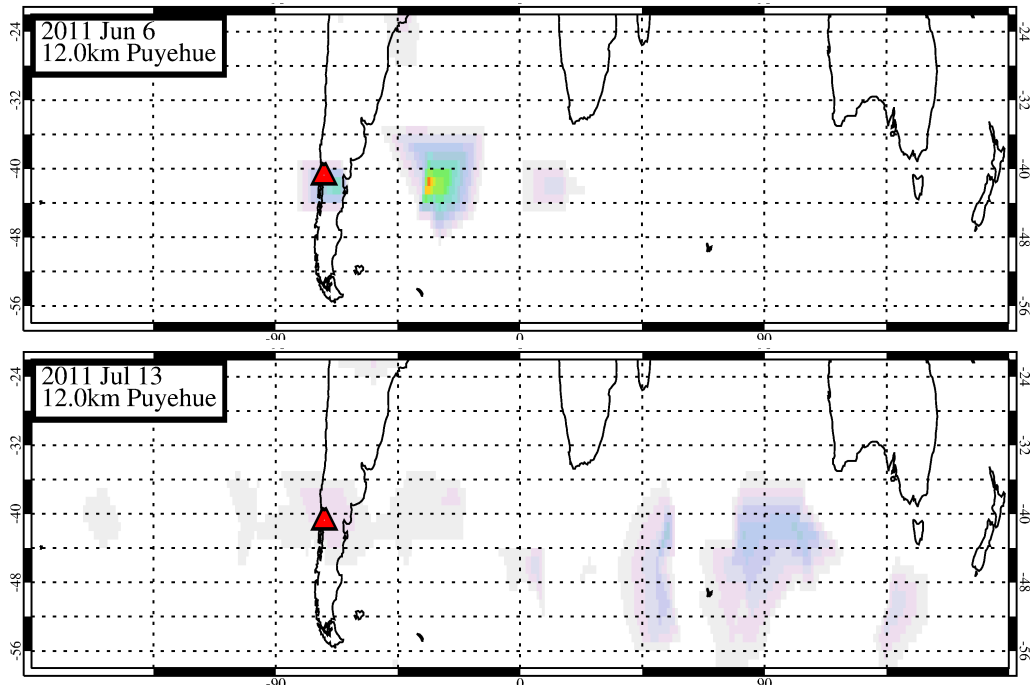
Figure 12: The spatial variation of the 1st volcanic singular vector's influence following the Puyehue eruption. Plots are from June 6th 2011 (upper) and July 13th 2011 (lower) between 60° S and 20° S at 12 km. The location of the volcano is marked with a red triangle. Data has been gridded and averaged to account for irregular sampling of the satellite. This irregular sampling is also responsible for the discontinuities in the plume in the upper figure where bands of clear sky are likely due to overpasses before the plume had extended across the South Atlantic Ocean. As time evolved the plume was seen to spread out spatially, become weaker in signal strength, and move from west to east, circling the world several times.

53
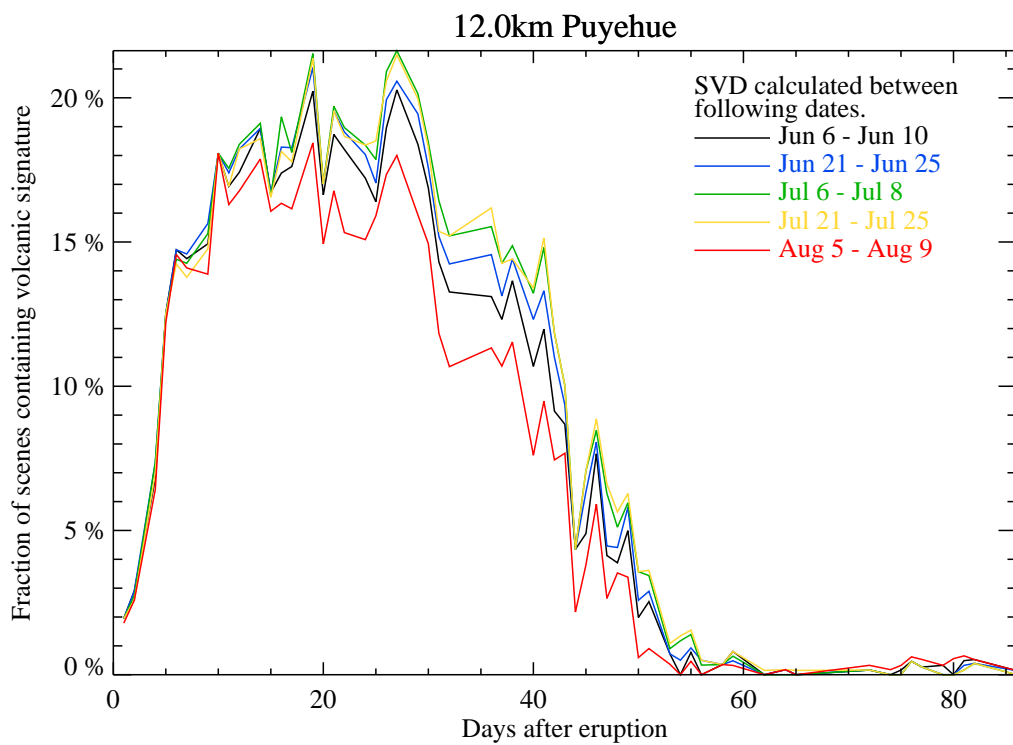
Figure 13: The spatial coverage of the Puyehue volcanic plume at 12 km for the geographical region shown in Figure 12. Coverage is calculated as the ratio of flagged profiles (where $\lambda_{\mathrm{volc},1}$ is significant) to all available profiles. The different coloured lines indicate volcanic singular vectors calculated during different measurement periods.

SVD$_{volc}$ #0 (Nabro, 15.0km)
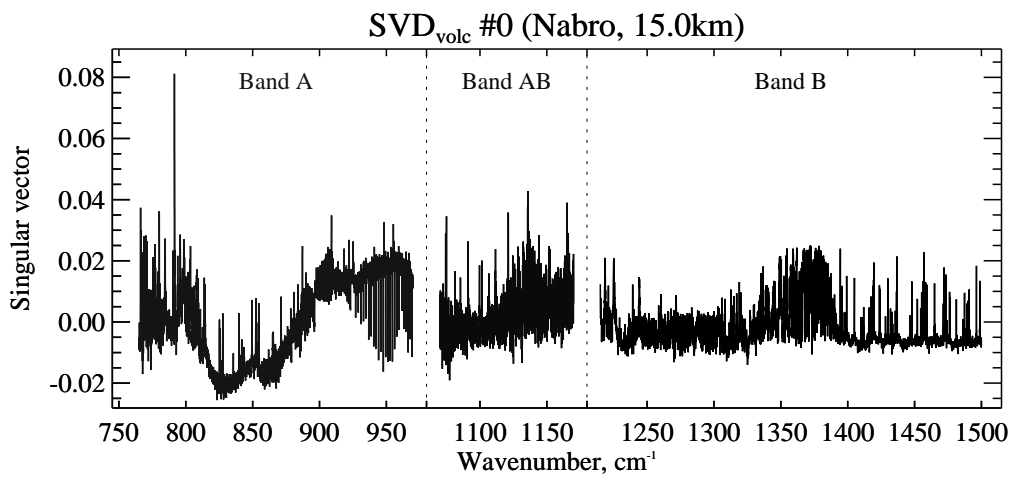
Figure 14: The principle singular volcanic singular vector for the Nabro eruption, calculated using data from the week after the eruptions, when the empirical flag defined in Equation 6 is positive. As with Figure 11, the three shortest MIPAS wavenumber bands, A, AB, and B were fitted, excluding the ozone region of AB band, and the beginning of the A band. Calculations were restricted to the latitude range 20-70° N. The SO$_2$ ν_1 and ν_2 absorption bands can be seen at 1152 cm^{-1} and 1362 cm^{-1}.
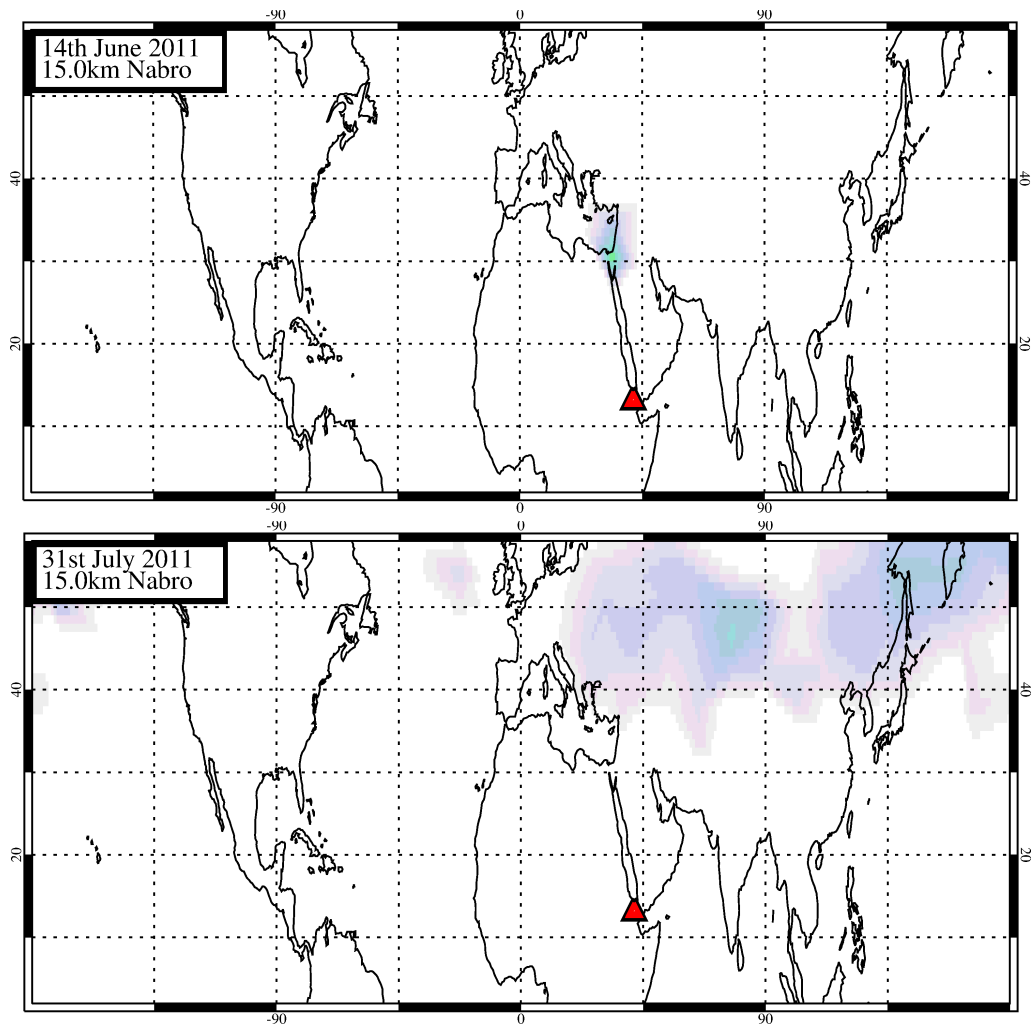
Figure 15: As Figure 12, but for the Nabro eruption. Significant volcanic signals between 30° N and 70° N at 15 ± 1.5 km are shown. Nabro is located at 13° N and is shown by the red triangle. The upper figure, showing the day after the eruption has the plume emerging. A month later (lower), the volcanic signature can be seen all over the northern hemisphere, more evenly but more weakly distributed.
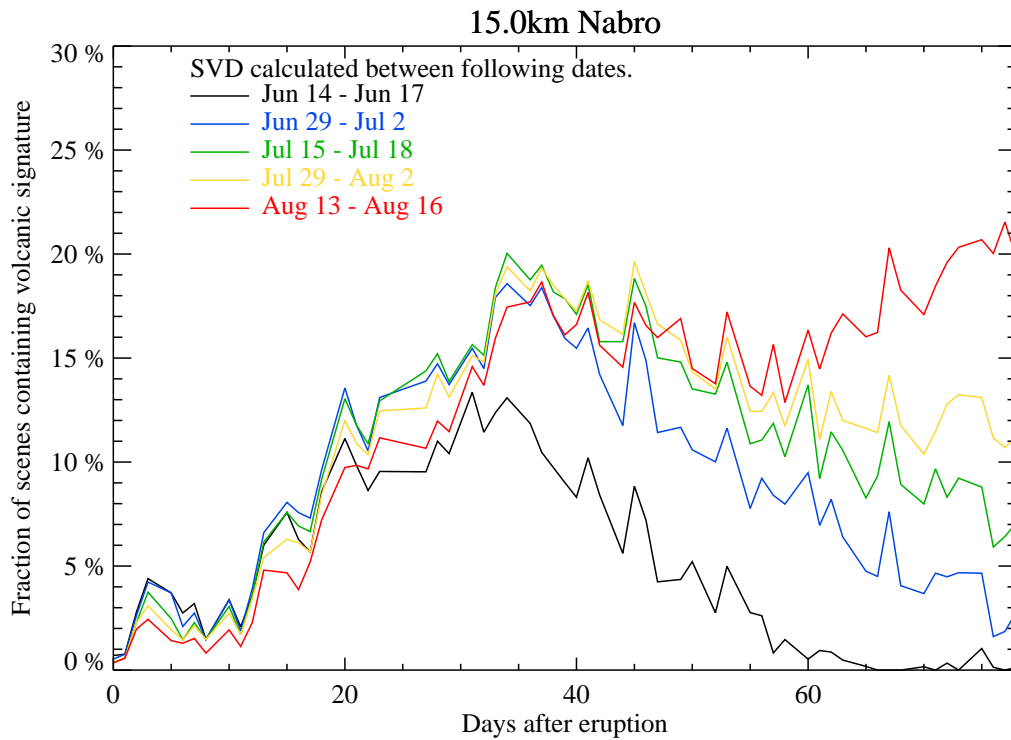
Figure 16: As Figure 13, but for a nominal altitude of 15 km and the Nabro geographical region shown in Figure 15.
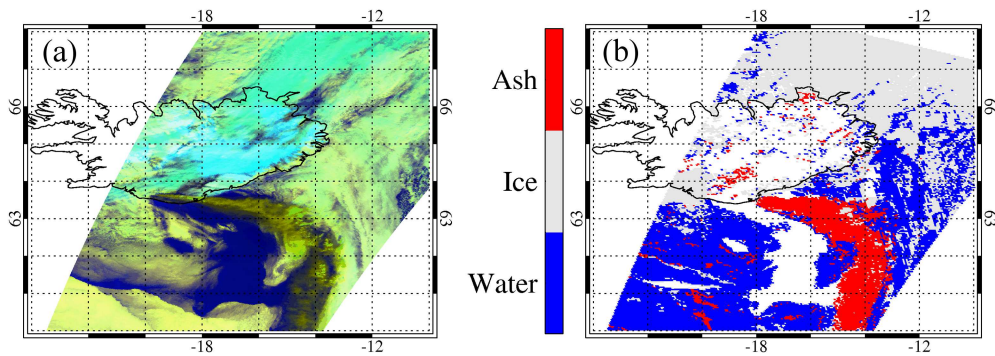
Figure 17: (a) A false colour image (designed to highlight volcanic ash as green-brown) of the Eyjafjallajökull eruption plume constructed from images acquired by AATSR at 12.13 GMT on the 6th May 2010. (b) Best fitting cloud type for the scene.
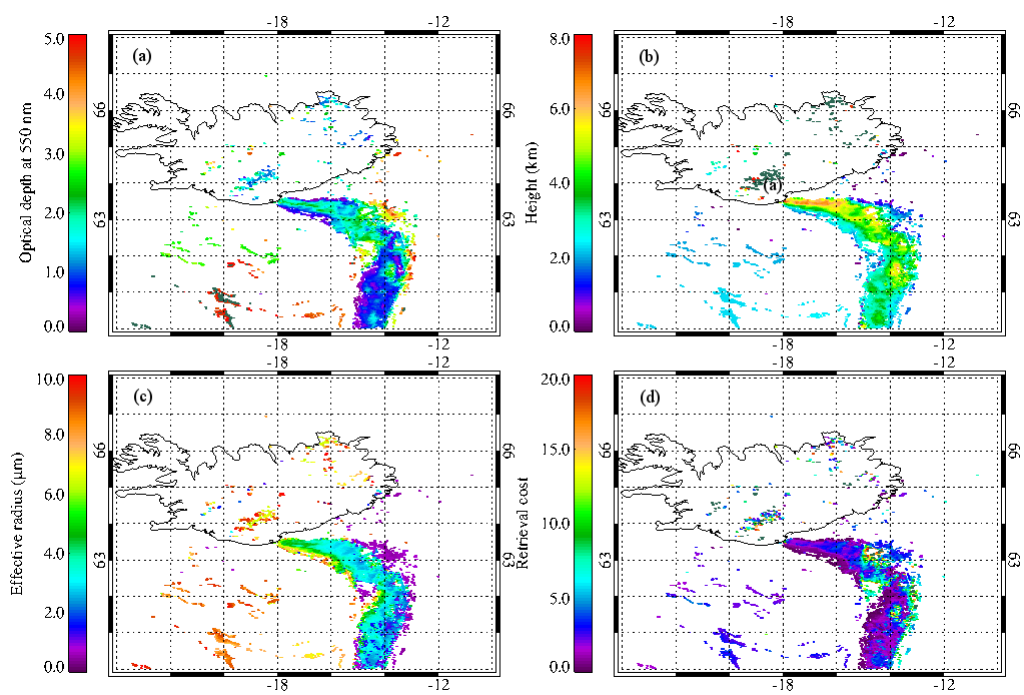
Figure 18: The retrieved (a) optical depth, (b) cloud-top height, (c) effective radius and (d) retrieval cost for those pixels identified as ash.
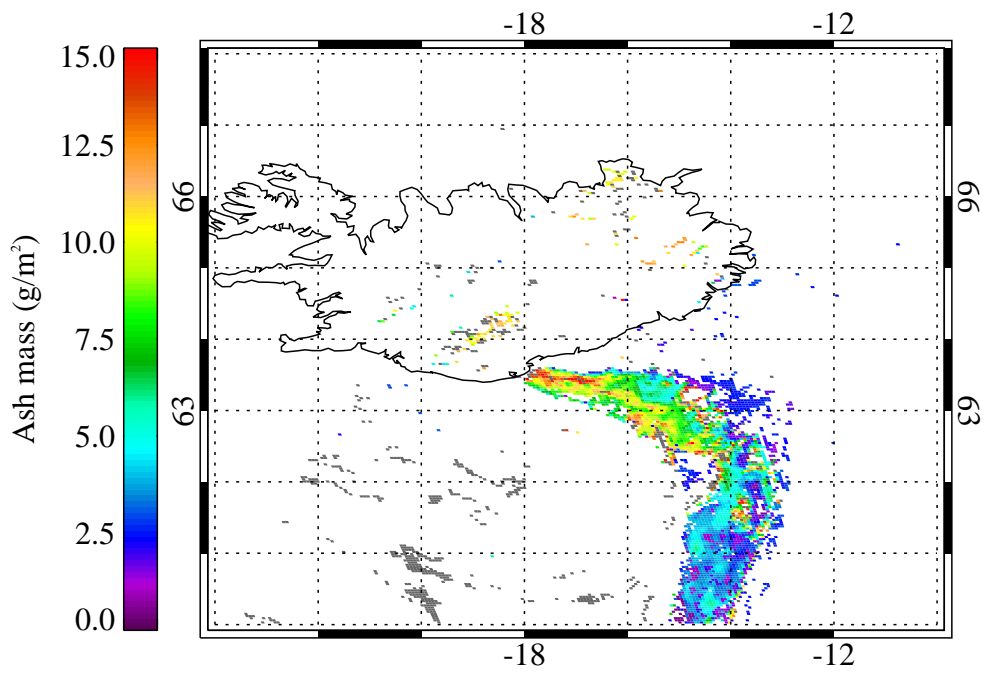
Figure 19: Ash mass density for the 6th May 2010.
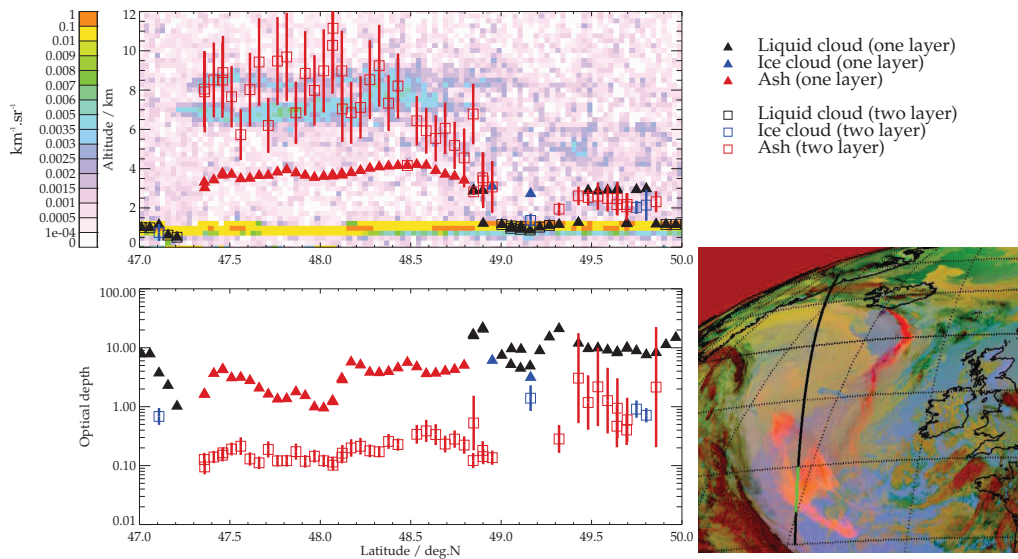
Figure 20: Example ORAC results for a SEVIRI scene at 14:00 UT on 7 May 2010, compared to co-incident CALIOP lidar observations. The top left-hand panel shows the CALIOP measured lidar back-scatter with the ORAC retrieved cloud-top height superimposed on top. As indicated in the legend, triangles show results from the single layer scheme and open squares show the height (of the upper layer) from the two-layer scheme. Error bars are shown in both cases though those from the single layer scheme are too small to be seen on this scale. Colours indicate the particle type which best matches observations. The bottom left-hand panel shows the retrieved optical depth. In the bottom-right is a false colour image from SEVIRI based on the 8.7, 11 and 12 μm channels, in which ash appears as bright red/orange or pink. The CALIOP track is shown as a black line, with the section shown in the left-hand panels highlight in green.